

¹ **Searches for Supersymmetry using the α_T**
² **variable with the CMS detector at the LHC**

³ Darren Burton

⁴ Imperial College London
⁵ Department of Physics

⁶ A thesis submitted to Imperial College London
⁷ for the degree of Doctor of Philosophy

Abstract

10

Declaration

11

I, the author of this thesis, declare that the work presented within this
document to be my own. The work presented in Chapters 3.4.1, 4 and 5
is a result of the authors own work or that of which I have been a major
contributor unless explicitly stated otherwise, and is carried out within the
context of the Imperial College London and CERN SUSY groups, itself a
subsection of the greater CMS collaboration. All figures and studies taken
from external sources are referenced appropriately throughout this document.

18

Darren Burton

19

Acknowledgements

20

Of the many people who deserve thanks, some are particularly prominent....

Preface

Contents

23	List of Figures	viii
24	List of Tables	xii
25	1. Introduction	2
26	2. A Theoretical Overview	5
27	2.1. The Standard Model	5
28	2.1.1. Gauge Symmetries of the SM	7
29	2.1.2. The Electroweak Sector and Electroweak Symmetry Breaking	9
30	2.2. Motivation for Physics Beyond the Standard Model	13
31	2.3. Supersymmetry Overview	15
32	2.3.1. R-Parity	16
33	2.4. Experimental signatures of SUSY at the LHC	17
34	2.4.1. Simplified Models	18
35	3. The LHC and the CMS Detector	20
36	3.1. The LHC	20
37	3.2. The CMS detector	23
38	3.2.1. Detector Subsystems	23
39	3.2.2. Tracker	24
40	3.2.3. Electromagnetic Calorimeter	25
41	3.2.4. Hadronic Calorimeter	26
42	3.2.5. Muon Systems	27
43	3.3. Event Reconstruction and Object Definition	28
44	3.3.1. Jets	28
45	3.3.2. B-tagging	30
46	3.4. Triggering System	32
47	3.4.1. The Level-1 Trigger	34

48	3.4.2. L1 Trigger Jet Algorithm	35
49	3.4.3. Measuring L1 Jet Trigger Efficiencies	36
50	3.4.4. Effects of the L1 Jet Seed	38
51	3.4.5. Robustness of L1 Jet Performance against Pile-up	41
52	3.4.6. Summary	43
53	4. SUSY searches in Hadronic Final States	45
54	4.1. The α_T search	46
55	4.1.1. The α_T variable	47
56	4.1.2. Search Strategy	50
57	4.1.3. Trigger Strategy	50
58	4.1.4. Event Selection	50
59	4.1.5. Background Estimation	50
60	4.1.6. Systematic Uncertainties on Transfer Factors	50
61	4.2. Searches for Natural SUSY with B-tag templates.	50
62	5. Results	51
63	5.1. Statistical Interpretation	51
64	5.2. Interpretation in Simplified Signal Models	51
65	A. Miscellaneous	52
66	A.1. Noise Filters	52
67	A.2. Primary Vertices	53
68	B. L1 Jets	54
69	B.1. Jet matching efficiencies	54
70	B.2. Leading Jet Energy Resolution	55
71	B.3. Resolution for Energy Sum Quantities	58
72	Bibliography	64

⁷³ List of Figures

⁷⁴ 2.1.	One loop quantum corrections to the Higgs squared mass parameter m_h^2 due to a fermion.	⁷⁵ 14
⁷⁶ 2.2.	Two example simplified model decay chains.	⁷⁶ 19
⁷⁷ 3.1.	A top down layout of the LHC, with the position of the four main detectors labelled.	⁷⁸ 21
⁷⁹ 3.2.	The total integrated luminosity delivered to and collected by Compact Muon Solenoid (CMS) during the 2012 8 TeV pp runs	⁸⁰ 22
⁸¹ 3.3.	A pictorial depiction of the CMS detector.	⁸² 24
⁸² 3.4.	Illustration of the CMS Electromagnetic CALorimeter (ECAL).	⁸³ 26
⁸³ 3.5.	Schematic of the CMS Hadronic CALorimeter (HCAL).	⁸⁴ 27
⁸⁴ 3.6.	Combined Secondary Vertex (CSV) algorithm discriminator values in enriched $t\bar{t}$ and inclusive multi jet samples	⁸⁵ 31
⁸⁶ 3.7.	Data/MC b-tag scale factors derived using the Combined Secondary Vertex Medium Working Point (CSVM) tagger.	⁸⁷ 32
⁸⁸ 3.8.	Data/MC mis-tag scale factors derived using the CSVM tagger.	⁸⁹ 33
⁸⁹ 3.9.	The CMS Level 1 Trigger (L1) Trigger system.	⁹⁰ 34
⁹⁰ 3.10.	Illustration of the Level-1 jet finding algorithm.	⁹¹ 36
⁹¹ 3.11.	L1 jet efficiency turn-on curves as a function of the offline CaloJet and PFJet E_T	⁹² 38
⁹³ 3.12.	L1 jet efficiency turn-on curves as a function of the offline CaloJet E_T for the 2012 run period B and C.	⁹⁴ 39

95	3.13. Trigger cross section for the L1HTT150 trigger path.	40
96	3.14. L1 H_T efficiency turn-on curves as a function of the offline CaloJet H_T	41
97	3.15. L1 jet efficiency turn-on curves as a function of the leading offline E_T Calo	
98	(left) and PF (right) jet, for low, medium and high pile-up conditions.	42
99	3.16. Fit values from an Exponentially Modified Gaussian (EMG) function fitted	
100	to the resolution plots of leading Calo jet E_T measured as a function of	
101	$\frac{(L1\ E_T - \text{Offline}\ E_T)}{\text{Offline}\ E_T}$ for low, medium and high pile-up conditions.	43
102	3.17. Fit values from an EMG function fitted to the resolution plots of leading	
103	PF jet E_T measured as a function of $\frac{(L1\ E_T - \text{Offline}\ E_T)}{\text{Offline}\ E_T}$ for low, medium and	
104	high pile-up conditions.	44
105	4.1. Reconstructed offline H_T for 11.7fb^{-1} of data after a basic pre-selection.	48
106	4.2. The event topologies of background QCD dijet events (right) and a generic	
107	SUPERSYmmetry (SUSY) signature with genuine \cancel{E}_T (left).	48
108	4.3. The α_T distributions for the low 2-3 (left) and high ≥ 4 (right) jet	
109	multiplicities after a full analysis selection and shown for $H_T > 375$	50
110	B.1. Leading jet matching efficiency as a function of the offline CaloJet E_T	54
111	B.2. Resolution plots of the leading offline Calo E_T measured as a function of	
112	$\frac{(L1\ E_T - \text{Offline}\ E_T)}{\text{Offline}\ E_T}$ for low (a), medium (b) and high (c) pile-up conditions.	56
113	B.3. Resolution plots of the leading off-line PF E_T measured as a function of	
114	$\frac{(L1\ E_T - \text{Offline}\ E_T)}{\text{Offline}\ E_T}$ for low (a), medium (b) and high (c) pile-up conditions.	58
115	B.4. $\sum E_T$ resolution parameters in bins of Calo $\sum E_T$ measured for the defined	
116	low, medium and high pile up conditions.	59
117	B.5. $\sum E_T$ resolution parameters in bins of PF $\sum E_T$ measured for the defined	
118	low, medium and high pile up conditions.	59
119	B.6. \cancel{E}_T resolution parameters in bins of Calo \cancel{E}_T measured for the defined	
120	low, medium and high pile up conditions.	60
121	B.7. \cancel{E}_T resolution parameters in bins of PF \cancel{E}_T measured for the defined low,	
122	medium and high pile up conditions.	60

123	B.8. H_T resolution parameters in bins of Calo H_T measured for the defined low, medium and high pile up conditions.	61
124		
125	B.9. H_T resolution parameters in bins of PF H_T measured for the defined low, medium and high pile up conditions.	61
126		
127	B.10. \mathcal{H}_T resolution parameters in bins of \mathcal{H}_T measured for the defined low, medium and high pile up conditions.	62
128		
129	B.11. \mathcal{H}_T resolution parameters in bins of PF \mathcal{H}_T measured for the defined low, medium and high pile up conditions.	62
130		

¹³¹ List of Tables

¹³²	2.1. The fundamental particles of the Standard Model (SM), with spin, charge and mass displayed.	6
¹³⁴	3.1. Results of a cumulative EMG function fit to the turn-on curves for L1 single jet triggers in 2012 Run Period C.	38
¹³⁶	3.2. Results of a cumulative EMG function fit to the turn-on curves for L1 single jet triggers in the 2012 run period B and C.	39
¹³⁸	3.3. Results of a cumulative EMG function fit to the turn-on curves for H_T in 2012 run period B and C.	40
¹⁴⁰	3.4. Results of a cumulative EMG function fit to the efficiency turn-on curves for L1 single jet triggers in the 2012 run period C, for low,medium and high pile-up conditions.	41
¹⁴³	3.5. Results of a cumulative EMG function fit to the efficiency turn-on curves for Level-1 single jet triggers in the 2012 run period C, for low,medium and high pile-up conditions.	42
¹⁴⁶	4.1. A summary of the Simplified Model Spectra (SMS) models interpreted in this analysis, involving both direct (D) and gluino-induced (G) production of squarks and their decays.	46
¹⁴⁹	B.1. Results of a cumulative EMG function fit to the turn-on curves for the matching efficiency of the leading jet in an event to a Level-1 jet in run 2012C and 2012B data.	55

“The Universe is about 1,000,000 years old.”

— Matthew Kenzie, 1987-present : Discoverer of the Higgs Boson.

Chapter 1.

¹⁵⁴ Introduction

¹⁵⁵ During the 20th century great advances have been made in our understanding of the
¹⁵⁶ universe, where it comes from, where it is going and what it is made of. The Standard
¹⁵⁷ Model (**SM**) first formulated in the 1960's is one of the crowning achievements in science's
¹⁵⁸ quest to explain the most fundamental processes and interactions that make up our
¹⁵⁹ universe. It has provided a highly successful explanation of a wide range of phenomena
¹⁶⁰ in Particle Physics and has stood up to extensive experimental scrutiny [1].

¹⁶¹ Despite it's successes it is not a complete theory, with significant questions remaining
¹⁶² unanswered. It describes only three of the four known forces with gravity not incorpo-
¹⁶³ rated within the framework of the **SM**. Cosmological experiments infer that just $\sim 4\%$
¹⁶⁴ of the observable universe exists as matter, with elusive "Dark Matter" accounting for a
¹⁶⁵ further $\sim 23\%$ [2]. However no particle predicted by the **SM** is able to account for it. At
¹⁶⁶ higher energy scales and small distances the (non-)unification of the fundamental forces
¹⁶⁷ point to problems with the **SM** at least at higher energies not yet probed experimentally.

¹⁶⁸ Many theories exist as extensions to the **SM** and predict a range of observables
¹⁶⁹ that can be detected at the Large Hadron Collider (**LHC**) of which SUperSYmmetry
¹⁷⁰ (**SUSY**) is one such example. It predicts a new symmetry of nature in which all current
¹⁷¹ particles in the **SM** would have a corresponding supersymmetric partner. Common to
¹⁷² most Supersymmetric theories is a stable, weakly interacting Lightest Supersymmetric
¹⁷³ Partner (**LSP**), which has the properties of a possible dark matter candidate. The **SM**
¹⁷⁴ and the main principles of Supersymmetric theories are outlined in Chapter 2, with
¹⁷⁵ emphasis on placed on how experimental signatures of **SUSY** may reveal themselves at
¹⁷⁶ the **LHC**.

177 The experimental goal of the **LHC** is to further test the framework of the **SM**,
178 exploring the TeV mass scale for the first time, and to seek a connection between the
179 particles produced in proton collisions and dark matter. The first new discovery by
180 this extraordinary machine was announced on the 4th of July 2012. The long-awaited
181 discovery was the culmination decades of experimental endeavours in the search for the
182 Higgs boson, providing an answer to the mechanism of electroweak symmetry breaking
183 within the **SM** [3][4].

184 This discovery was made possible through data taken by the two multi purpose
185 detectors (**CMS** and A Toroidal LHC ApparatuS (**ATLAS**)) located on the **LHC** ring.
186 An experimental description of the **CMS** detector and the **LHC** is described in Chapter 3,
187 including some of the object reconstruction used by **CMS** in searches for **SUSY** signatures.
188 The performance of the **CMS** Level-1 calorimeter trigger, benchmarked by the author is
189 also included within this chapter.

190 The analysis conducted by the author is detailed within Chapter 4. This chapter
191 contains a description of the search for evidence of the production of Supersymmetric
192 particles at the **LHC**. The main basis of the search centres around the kinematic
193 dimensionless α_T variable, which provides strong rejection of backgrounds with fake
194 missing energy signatures whilst maintaining good sensitivity to a variety of **SUSY**
195 topologies. The author's work as an integral part of the analysis group is documented in
196 detail, which has culminated in numerous publications over the past two years. The latest
197 of which was published in the European Physical Journal C (**EPJC**) [5] and contains the
198 results which are discussed within this and the sequential Chapter.

199 The author in particular has played a major role in the extension of the α_T analysis into
200 the additional b-tagged and jet multiplicity dimensions increasing the sensitivity of the
201 analysis to a range of **SUSY** topologies. Additionally the author has worked extensively
202 in both increasing the statistical precision of electroweak predictions measured from
203 simulation through analytical techniques, and the derivation of a data driven systematic
204 uncertainty through the establishment of closure tests within the control samples of the
205 analysis.

206 Also included within this Chapter is a method to search for **SUSY** signatures which
207 are rich in top and bottom flavoured jet final states. A parametrisation of the b-tagging
208 distribution for different Electroweak processes is used to establish templates, which
209 are then used to estimate the expected number of 3 or 4 b-tagged jet events from **SM**

210 processes. The α_T search is used as a cross check for this template method to establish
211 it's functionality.

212 Finally the interpretation of such results within the framework of a variety of Simplified
213 Model Spectra (**SMS**), which describe an array of possible **SUSY** event topologies is
214 documented in Chapter 5. A description of the statistical model used to derive these
215 interpretations and the possible implications of the results presented in this thesis is
216 discussed within this Chapter. Natural units are used throughout this thesis in which \hbar
217 = c = 1.

Chapter 2.

²¹⁸ A Theoretical Overview

²¹⁹ Within this chapter, a brief introduction and background to the **SM** is given. Its success
²²⁰ as a rigorously tested and widely accepted theory is discussed as well as the deficiencies
²²¹ with this theory that hint there this theory is not a complete description of our universe.
²²² The motivations for new physics at the TeV scale and in particular Supersymmetric
²²³ theories are outlined within Section (2.3), with the chapter concluding with how an
²²⁴ experimental signature of such theories can be produced and observed at the **LHC**,
²²⁵ Section (2.4).

²²⁶ 2.1. The Standard Model

²²⁷ The **SM** is the name given to the relativistic Quantum Field Theory (**QFT**), where
²²⁸ particles are represented as excitations of fields, which describes the interactions and
²²⁹ properties of all the known elementary particles [6][7][8][9]. It is a renormalisable field
²³⁰ theory which contains three symmetries: $SU(3)$ for colour charge, $SU(2)$ for weak isospin
²³¹ and $U(1)$ relating to weak hyper charge, which require its Lagrangian \mathcal{L}_{SM} to be invariant
²³² under local gauge transformation.

²³³ Within the **SM** theory, matter is composed of spin $\frac{1}{2}$ fermions, which interact with each
²³⁴ other via the exchange of spin-1 gauge bosons. A summary of the known fundamental
²³⁵ fermions and bosons is given in Table 2.1.

²³⁶ Fermions are separated into quarks and leptons of which only quarks interact with
²³⁷ the strong nuclear force. Quarks unlike leptons are not seen as free particles in nature,
²³⁸ but rather exist only within baryons, composed of three quarks with an overall integer

Particle	Symbol	Spin	Charge	Mass (GeV)
First Generation Fermions				
Electron Neutrino	ν_e	$\frac{1}{2}$	0	$< 2.2 \times 10^{-6}$
Electron	e	$\frac{1}{2}$	-1	0.51×10^{-3}
Up Quark	u	$\frac{1}{2}$	$\frac{2}{3}$	$2.3^{+0.7}_{-0.5} \times 10^{-3}$
Down Quark	d	$\frac{1}{2}$	$-\frac{1}{3}$	$4.8^{+0.7}_{-0.3} \times 10^{-3}$
Second Generation Fermions				
Muon Neutrino	ν_μ	$\frac{1}{2}$	0	-
Muon	μ	$\frac{1}{2}$	-1	1.05×10^{-3}
Charm Quark	c	$\frac{1}{2}$	$\frac{2}{3}$	1.275 ± 0.025
Strange Quark	s	$\frac{1}{2}$	$-\frac{1}{3}$	$95 \pm 5 \times 10^{-3}$
Third Generation Fermions				
Tau Neutrino	ν_τ	$\frac{1}{2}$	0	-
Tau	τ	$\frac{1}{2}$	-1	1.77
Top Quark	t	$\frac{1}{2}$	$\frac{2}{3}$	173.5 ± 0.8
Bottom Quark	b	$\frac{1}{2}$	$-\frac{1}{3}$	4.65 ± 0.03
Gauge Bosons				
Photon	γ	1	0	0
W Boson	W^\pm	1	± 1	80.385 ± 0.015
Z Boson	Z	1	0	91.187 ± 0.002
Gluons	g	1	0	0
Higgs Boson	H	0	0	125.3 ± 0.5 [4]

Table 2.1.: The fundamental particles of the SM, with spin, charge and mass displayed. Latest mass measurements taken from [1].

²³⁹ charge, and quark-anti-quark pairs called mesons. Both leptons and quarks are grouped
²⁴⁰ into three generations which have the same properties, but with ascending mass in each
²⁴¹ subsequent generation.

²⁴² The gauge bosons mediate the interactions between fermions. The field theories
²⁴³ of Quantum Electro-Dynamics (QED) and Quantum Chromo-Dynamics (QCD), yield
²⁴⁴ massless mediator bosons, the photon and eight coloured gluons which are consequences
²⁴⁵ of the gauge invariance of those theories, detailed in Section (2.1.1).

²⁴⁶ The unification of the electromagnetic and weak-nuclear forces into the current
²⁴⁷ Electroweak theory yield the weak gauge bosons, W^\pm and Z through the mixing of the
²⁴⁸ associated gauge fields. The force carriers of this theory were experimentally detected by

249 the observation of weak neutral current, discovered in 1973 in the Gargamelle bubble
250 chamber located at European Organization for Nuclear Research (**CERN**) [10], with the
251 masses of and the weak gauge bosons measured by the UA1 and U2 experiments at the
252 Super Proton Synchrotron (**SPS**) collider in 1983 [11][12].

253 2.1.1. Gauge Symmetries of the SM

254 Symmetries are of fundamental importance in the description of physical phenomena.
255 Noether's theorem states that for a dynamical system, the consequence of any symmetry
256 is an associated conserved quantity [13]. Invariance under translations, rotations, and
257 Lorentz transformations in physical systems lead to conservation of momentum, energy
258 and angular momentum.

259 In the **SM**, a quantum theory described by Lagrangian formalism, the weak, strong and
260 electromagnetic interactions are described in terms of “gauge theories”. A gauge theory
261 possesses invariance under a set of “local transformations”, which are transformations
262 whose parameters are space-time dependent. The requirement of gauge invariance within
263 the **SM** necessitates the introduction of force-mediating gauge bosons and interactions
264 between fermions and the bosons themselves. Given the nature of the topics covered by
265 this thesis, the formulation of Electroweak Sector (**EWK**) within the **SM** Lagrangian is
266 reviewed within this section.

267 The simplest example of the application of the principle of local gauge invariance
268 within the **SM** is in Quantum Electro-Dynamics (**QED**), the consequences of which
269 require a massless photon field [14][15].

270 Starting from the free Dirac Lagrangian written as

$$\mathcal{L} = \bar{\psi}(i\gamma^\mu \partial_\mu - m)\psi, \quad (2.1)$$

271 where ψ represents a free non interacting fermionic field, with the matrices $\gamma^\mu, \mu \in$
272 $0, 1, 2, 3$ defined by the anti commutator relationship $\gamma^\mu \gamma^\nu + \gamma^\nu \gamma^\mu = 2\eta^{\mu\nu} I_4$ where $\eta^{\mu\nu}$ is
273 the flat space-time metric $(+, -, -, -)$ and I_4 is the 4×4 identity matrix.

274 Under a local U(1) abelian gauge transformation in which ψ transforms as:

$$\psi(x) \rightarrow \psi'(x) = e^{i\theta(x)}\psi(x) \quad \bar{\psi}(x) \rightarrow \bar{\psi}'(x) = e^{i\theta(x)}\bar{\psi}(x) \quad (2.2)$$

275 the kinetic term of the Lagrangian does not remain invariant, due to the partial
276 derivative interposed between the $\bar{\psi}$ and ψ yielding,

$$\partial_\mu \psi \rightarrow e^{i\theta(x)} \partial_\mu \psi + i e^{i\theta(x)} \psi \partial_\mu \theta. \quad (2.3)$$

277 To ensure that \mathcal{L} remains invariant, a modified derivative, D_μ , that transforms
278 covariantly under phase transformations is introduced. In doing this a vector field A_μ
279 with transformation properties that cancel out the unwanted term in (2.3) must also be
280 included,

$$D_\mu \equiv \partial_\mu - ieA_\mu, \quad A_\mu \rightarrow A_\mu + \frac{1}{e} \partial_\mu \theta. \quad (2.4)$$

281 Invariance of the Lagrangian is then achieved by replacing ∂_μ by D_μ :

$$\begin{aligned} \mathcal{L} &= i\bar{\psi}\gamma^\mu D_\mu \psi - m\bar{\psi}\psi \\ &= \bar{\psi}(i\gamma^\mu \partial_\mu - m)\psi + e\bar{\psi}\gamma^\mu \psi A_\mu \end{aligned} \quad (2.5)$$

282 An additional interaction term is now present in the Lagrangian, coupling the Dirac
283 particle to this vector field, which is interpreted as the photon in QED. To regard this
284 new field as the physical photon field, a term corresponding to its kinetic energy must be
285 added to the Lagrangian from Equation (2.5). Since this term must also be invariant
286 under the conditions of Equation (2.4), it is defined in the form $F_{\mu\nu} = \partial^\mu A^\nu - \partial^\nu A^\mu$.

287 This then leads to the Lagrangian of QED:

$$\mathcal{L}_{QED} = \underbrace{i\bar{\psi}\gamma^\mu\partial_\mu\psi - \frac{1}{4}F_{\mu\nu}F^{\mu\nu}}_{\text{kinetic term}} + \underbrace{m\bar{\psi}\psi}_{\text{mass term}} + \underbrace{e\bar{\psi}\gamma^\mu\psi A_\mu}_{\text{interaction term}} \quad (2.6)$$

Within the Lagrangian there remains no mass term of the form $m^2A_\mu A^\mu$, which is prohibited by gauge invariance. This implies that the gauge particle, the photon, must be massless.

2.1.2. The Electroweak Sector and Electroweak Symmetry Breaking

The same application of gauge symmetry and the requirement of local gauge invariance can be used to unify QED and the Weak force in the Electroweak Sector (EWK). The nature of EWK interactions is encompassed within a Lagrangian invariant under transformations of the group $SU(2)_L \times U(1)_Y$.

The weak interactions from experimental observation [16], are known to violate parity and are therefore not symmetric under interchange of left and right helicity fermions. Thus within the SM the left and right handed parts of these fermion fields are treated separately. A fermion field is then split into two left and right handed chiral components, $\psi = \psi_L + \psi_R$, where $\psi_{L/R} = (1 \pm \gamma^5)\psi$.

The $SU(2)_L$ group is the special unitary group of 2×2 matrices U satisfying $UU^\dagger = I$ and $\det(U) = 1$. It may be written in the form $U = e^{-i\omega_i T_i}$, with the generators of the group $T_i = \frac{1}{2}\tau_i$ where τ_i , $i \in 1,2,3$ being the 2×2 Pauli matrices

$$\tau_1 = \begin{pmatrix} 0 & 1 \\ 1 & 0 \end{pmatrix} \quad \tau_2 = \begin{pmatrix} 0 & -i \\ i & 0 \end{pmatrix} \quad \tau_3 = \begin{pmatrix} 1 & 0 \\ 0 & -1 \end{pmatrix}, \quad (2.7)$$

which form a non Abelian group obeying the commutation relation $[T^a, T^b] \equiv if^{abc}T^c \neq 0$. The gauge fields that accompany this group are represented by $\hat{W}_\mu = (\hat{W}_\mu^1, \hat{W}_\mu^2, \hat{W}_\mu^3)$ and act only on the left handed component of the fermion field ψ_L .

308 One additional generator Y which represents the hypercharge of the particle under
309 consideration is introduced through the $U(1)_Y$ group acting on both components of the
310 fermion field, with an associated vector boson field \hat{B}_μ .

311 The $SU(2)_L \times U(1)_Y$ transformations of the left and right handed components of ψ
312 are summarised by,

$$\begin{aligned}\chi_L &\rightarrow \chi'_L = e^{i\theta(x) \cdot T + i\theta(x)Y} \chi_L, \\ \psi_R &\rightarrow \psi'_R = e^{i\theta(x)Y} \psi_R,\end{aligned}\tag{2.8}$$

313 where the left handed fermions form isospin doubles χ_L and the right handed fermions
314 are isosinglets ψ_R . For the first generation of leptons and quarks this represents

$$\begin{aligned}\chi_L &= \begin{pmatrix} \nu_e \\ e \end{pmatrix}_L, & \begin{pmatrix} u \\ d \end{pmatrix}_L \\ \psi_R &= e_R, & u_R, d_R\end{aligned}\tag{2.9}$$

315 Imposing local gauge invariance within \mathcal{L}_{EWK} is once again achieved by modifying
316 the covariant derivative

$$D_\mu = \partial_\mu - \frac{ig}{2} \tau^i W_\mu^i - \frac{ig'}{2} Y B_\mu,\tag{2.10}$$

317 where g and g' are the coupling constant of the $SU(2)_L$ and $U(1)_Y$ groups respectively.
318 Taking the example of the first generation of fermions defined in Equation.(2.9), with input
319 hypercharge values of -1 and -2 for χ_L and e_R respectively, would lead to a Lagrangian
320 \mathcal{L}_1 of the form,

$$\begin{aligned}\mathcal{L}_1 = &\bar{\chi}_L \gamma^\mu [i\partial_\mu - g \frac{1}{2} \tau \cdot W_\mu - g' (-\frac{1}{2}) B_\mu] \chi_L \\ &+ \bar{e}_R \gamma^\mu [i\partial_\mu - g' (-1) B_\mu] e_R - \frac{1}{4} W_{\mu\nu} \cdot W^{\mu\nu} - \frac{1}{4} B_{\mu\nu} B^{\mu\nu}.\end{aligned}\tag{2.11}$$

321 As in **QED**, these additional gauge fields introduce field strength tensors $B_{\mu\nu}$ and
322 $W_{\mu\nu}$,

$$\hat{B}_{\mu\nu} = \partial_\mu \hat{B}_\nu - \partial_\nu \hat{B}_\mu \quad (2.12)$$

$$\hat{W}_{\mu\nu} = \partial_\mu \hat{W}_\nu - \partial_\nu \hat{W}_\mu - g \hat{W}_\mu \times \hat{W}_\nu \quad (2.13)$$

323 corresponding to the kinetic energy and self coupling of the W_μ fields and the kinetic
324 energy term of the B_μ field.

325 None of these gauge bosons are physical particles, and instead linear combinations of
326 these gauge bosons make up γ and the W and Z bosons, defined as

$$W^\pm = \frac{1}{\sqrt{2}} (W_\mu^1 \mp i W_\mu^2) \quad \begin{pmatrix} Z_\mu \\ A_\mu \end{pmatrix} = \begin{pmatrix} \cos\theta_W & -\sin\theta_W \\ \sin\theta_W & \cos\theta_W \end{pmatrix} \begin{pmatrix} W_\mu^3 \\ B_\mu \end{pmatrix} \quad (2.14)$$

327 where the mixing angle, $\theta_w = \tan^{-1} \frac{g'}{g}$, relates the coupling of the neutral weak and
328 electromagnetic interactions.

329 As in the case of the formulation of the **QED** Lagrangian there remains no mass term
330 for the photon. However this is also the case for the W, Z and fermions in the Lagrangian,
331 contrary to experimental measurement. Any explicit introduction of mass terms would
332 break the symmetry of the Lagrangian and instead mass terms can be introduced through
333 spontaneous breaking of the **EWK** symmetry via the Higgs mechanism.

334 The Higgs mechanism induces spontaneous symmetry breaking through the introduc-
335 tion of a complex scalar SU(2) doublet field ϕ which attains a non-zero Vacuum
336 Expectation Value (**VEV**) [17][18][19][20].

$$\phi = \begin{pmatrix} \phi^+ \\ \phi^0 \end{pmatrix} \quad \text{with} \quad \begin{aligned} \phi^+ &\equiv (\phi_1 + i\phi_2)/\sqrt{2} \\ \phi^0 &\equiv (\phi_3 + i\phi_4)/\sqrt{2} \end{aligned} \quad (2.15)$$

337 The Lagrangian defined in Equation (2.11) attains an additional term \mathcal{L}_{Higgs} of the
338 form

$$\mathcal{L}_{Higgs} = \overbrace{(D_\mu \phi)^\dagger (D^\mu \phi)}^{\text{kinetic}} - \overbrace{\mu^2 \phi^\dagger \phi - \lambda (\phi^\dagger \phi)^2}^{\text{potential } V(\phi)} \quad (\mu^2, \lambda) > 0 \in \mathbb{R},$$

$$\mathcal{L}_{SM} = \mathcal{L}_{EWK} + \mathcal{L}_{Higgs}, \quad (2.16)$$

339 where the covariant derivative D_μ is that defined in Equation (2.10). The last two
340 terms of \mathcal{L}_{Higgs} correspond to the Higgs potential, in which positive real positive values
341 of μ^2 and λ are required to ensure the generation of masses for the bosons and leptons.
342 The minimum of this potential is found at $\phi^\dagger \phi = \frac{1}{2}(\phi_1^2 + \phi_2^2 + \phi_3^2 + \phi_4^2) = \mu^2/\lambda = v^2$,
343 where v represents the **VEV**.

344 Defining the ground state of the ϕ field to be consistent with the $V(\phi)$ minimum, and
345 then expanding around a ground state chosen to maintain an unbroken electromagnetic
346 symmetry thus preserving a zero photon mass [21] leads to

$$\phi_0 = \sqrt{\frac{1}{2}} \begin{pmatrix} 0 \\ v \end{pmatrix}, \quad \phi(x) = e^{i\tau \cdot \theta(x)/v} \sqrt{\frac{1}{2}} \begin{pmatrix} 0 \\ v + h(x) \end{pmatrix}, \quad (2.17)$$

347 where the fluctuations from the vacuum ϕ_0 are parametrized in terms of four real
348 fields, $\theta_1, \theta_2, \theta_3$ and $h(x)$.

349 Choosing to gauge away the three massless Goldstone boson fields by setting $\theta(x)$ to
350 zero and substituting $\phi(x)$ back into kinetic term of \mathcal{L}_{Higgs} from Equation (2.16) leads to
351 mass terms for the W^\pm and Z bosons

$$(D_\mu \phi)^\dagger (D^\mu \phi) = \frac{1}{2}(\partial_\mu h)^2 + \frac{g^2 v^2}{2} W_\mu^+ W^{-\mu} + \frac{v^2 g^2}{8 \cos^2 \theta_w} Z_\mu Z^\mu + 0 A_\mu A^\mu, \quad (2.18)$$

352 where the relations between the physical and electroweak gauge fields from Equation
353 (2.14) are used. The W^\pm and Z bosons can then be determined to be

$$M_W = \frac{1}{2}gv \quad M_Z = \frac{1}{2} \frac{gv}{\cos \theta_w}. \quad (2.19)$$

354 This mechanism is also used to generate fermion masses by introducing a Yukawa
 355 coupling between the fermions and the ϕ field [22], with the coupling strength of a particle
 356 to the ϕ field governing its mass. Additionally a scalar boson h with mass $m_h = v\sqrt{\frac{\lambda}{2}}$, is
 357 also predicted as a result of this spontaneous symmetry breaking and became known as
 358 the Higgs boson. Its discovery by the CMS and ATLAS experiments in 2012 is concrete
 359 evidence to support this method of mass generation within the SM.

360 2.2. Motivation for Physics Beyond the Standard 361 Model

362 As has been described, the SM has proved to be a very successful theory, predicting the
 363 existence of the W^\pm and Z bosons and the top quark long before they were experimentally
 364 observed. However the theory does not accurately describe all observed phenomena and
 365 has some fundamental theoretical flaws that hint at the need for additional extensions to
 366 the current theory.

367 On a theoretical level, the SM is unable to incorporate the gravitational interactions
 368 of fundamental particles within the theory. Whilst at the electroweak energy scales the
 369 relative strength of gravity is negligible compared to the other three fundamental forces,
 370 at much higher energy scales $M_{planck} \sim 10^{18} GeV$ quantum gravitational effects become
 371 increasingly dominant. The failure to reconcile gravity within the SM, demonstrates that
 372 the SM must become invalid at some higher energy scale.

373 Some other deficiencies with the SM include the fact that the predicted rate of
 374 Charge-Parity violation does not account for the matter dominated universe which we
 375 inhabit, and the SM prediction of zero neutrino mass conflicts with the observation of
 376 neutrino flavour mixing, attributed to mixing between neutrino mass eigenstates [23][24].

377 Perhaps one of the most glaring gaps in the predictive power of the SM is that there
 378 exists no candidate to explain the cosmic dark matter observed in galactic structures
 379 through indirect techniques including gravitational lensing and measurement of the
 380 orbital velocity of stars in galactic edges. Any such candidate must be very weakly

381 interacting which must also be stable, owing to the lack of direct detection of the decay
382 products of such an process. Providing a dark matter candidate is of the prime goals
383 which be tackled by any Beyond Standard Model (**BSM**) physics model.

384 The recent discovery of the Higgs boson whilst a significant victory for the predictive
385 power of the **SM**, brings with it still unresolved questions. This issue is commonly
386 described as the “hierarchy problem”.

387 In the absence of new physics between the TeV and Planck scale, calculating beyond
388 tree-level contributions to the Higgs mass term given by its self interaction, result in
389 divergent terms that push the Higgs mass up to the planck mass M_{planck} .

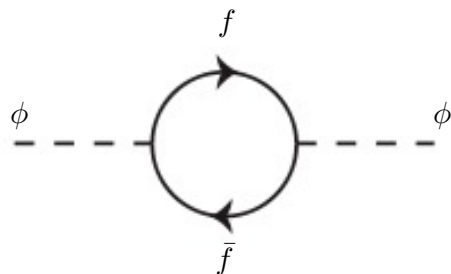


Figure 2.1.: One loop quantum corrections to the Higgs squared mass parameter m_h^2 due to a fermion.

390 This can be demonstrated by considering the one loop quantum correction to the
391 Higgs mass with a fermion f , shown in Figure 2.1 with mass m_f . The Higgs field couples
392 to f with a term in the Lagrangian $-\lambda_f h \bar{f} f$, yielding a correction of the form [25],

$$\delta m_h^2 = -\frac{|\lambda_f|^2}{8\pi^2} \Lambda^2 + \dots, \quad (2.20)$$

393 where λ_f represents the coupling strength for each type of fermion $\propto m_f$, and Λ the
394 cutoff energy scale at which the **SM** ceases to be a valid theory.

395 To recover the mass of the now discovered Higgs boson would require a fine-tuning of
396 the parameters to cancel out these mass corrections the the Higgs mass to the scale of
397 30 orders of magnitude. This appears as an unnatural solution to physicists and it is
398 this hierarchy problem that provides one of the strongest motivations for the theory of
399 SUperSYmmetry (**SUSY**).

⁴⁰⁰ 2.3. Supersymmetry Overview

⁴⁰¹ Supersymmetry provides potential solutions to many of the issues raised in the previous
⁴⁰² section. It provides a dark matter candidate, can explain baryogenesis in the early
⁴⁰³ universe and also provides an elegant solution to the hierarchy problem [26][27][28][29].
⁴⁰⁴ At its heart it represents a new space-time symmetry that relates fermions and bosons.
⁴⁰⁵ This symmetry converts bosonic states into fermionic states, and vice versa, see Equation
⁴⁰⁶ (2.21) ,

$$Q|Boson\rangle = |Fermion\rangle \quad Q|Fermion\rangle = |Boson\rangle, \quad (2.21)$$

⁴⁰⁷ where the operator Q is the generator of these transformations. Quantum field theories
⁴⁰⁸ which are invariant under such transformations are called supersymmetric.

⁴⁰⁹ This symmetry operator therefore acts upon a particles spin altering it by a half integer
⁴¹⁰ value. The consequences of the introduction of this additional space-time symmetry
⁴¹¹ introduce a new rich phenomenology. For example in supersymmetric theories, both
⁴¹² the left handed $SU(2)$ doublet and right handed singlet of fermions will have a spin-0
⁴¹³ superpartner, containing the same electric charge, weak isospin, and colour as its **SM**
⁴¹⁴ partner. In the case of the leptons $(\nu_l, l)_L$ will have two superpartners, a sneutrino $\tilde{\nu}_l{}_L$
⁴¹⁵ and a slepton \tilde{l}_L , whilst the singlet l_R also has a superpartner slepton \tilde{l}_R .

⁴¹⁶ Each particle in a supersymmetric theory is paired together with their superpartners
⁴¹⁷ as a result of this supersymmetric transformations in a so called supermultiplet. These
⁴¹⁸ superpartners will then consequently also contribute to the corrections to the Higgs mass.
⁴¹⁹ Bosonic and fermionic loops contributing to the correction appear with opposite signs,
⁴²⁰ and therefore cancellation of these divergent terms will stabilise the Higgs mass, solving
⁴²¹ the hierarchy problem [30][31].

⁴²² One of the simplest forms of **SUSY** would predict a whole set of supersymmetric
⁴²³ partners to their **SM** counterparts with the same mass and interactions. However the
⁴²⁴ currently lack of any experimental evidence for the predicted sparticle spectrum implies
⁴²⁵ **SUSY** must be a broken symmetry in which any sparticle masses must be greater than
⁴²⁶ their SM counterparts.

⁴²⁷ There exist many techniques which can induce supersymmetric breaking [32][33][34].
⁴²⁸ Of particular interest to experimental physicists are those at which the breaking scale

⁴²⁹ is of an order that is experimentally accessible to the LHC i.e. \sim TeV scale. Whilst
⁴³⁰ there is no requirement for supersymmetric breaking to occur at this energy scale, for
⁴³¹ supersymmetry to provide a solution to the hierarchy problem, it is necessary for this
⁴³² scale to not differ too drastically from the EWK scale [35][36].

⁴³³ 2.3.1. R-Parity

⁴³⁴ Some supersymmetric theories also present a solution to the dark matter problem. Such
⁴³⁵ theories can contain a Lightest Supersymmetric Partner (LSP), which matches the criteria
⁴³⁶ of a Weakly Interacting Massive Particle (WIMP) required by cosmological observation
⁴³⁷ if R-parity is conserved.

⁴³⁸ Baryon (B) and Lepton (L) number conservation is forbidden in the SM by renor-
⁴³⁹ malisability requirements. The violation of Baryon or Lepton number would result in
⁴⁴⁰ the proton lifetime much shorter than those set by experimental limits [37]. Another
⁴⁴¹ symmetry called R-parity is then often introduced to SUSY theories to maintain baryon
⁴⁴² and lepton conservation.

⁴⁴³ R-parity is described by the equation

$$R_P = (-1)^{3(B-L)+2s}, \quad (2.22)$$

⁴⁴⁴ where s represents the spin of the particles. $B = \pm \frac{1}{3}$ for quarks/antiquarks and $B = 0$
⁴⁴⁵ for all others, $L = \pm 1$ for leptons/antileptons, $L = 0$ for all others.

⁴⁴⁶ R-parity ensures the stability of the proton in SUSY models, and also has other
⁴⁴⁷ consequences for the production and decay of supersymmetric particles. At particle
⁴⁴⁸ colliders supersymmetric particles can only be pair produced, and similarly the decay
⁴⁴⁹ of any produced supersymmetric particle is restricted to a SM particle and a lighter
⁴⁵⁰ supersymmetric particle as allowed by conservation laws. A further implication of R-
⁴⁵¹ parity is that once a supersymmetric particle has decayed to the LSP it remains stable,
⁴⁵² unable to decay into a SM particle.

⁴⁵³ A LSP would not interact in a detector at a particle collider, leaving behind a missing
⁴⁵⁴ energy \cancel{E}_T signature. The assumption of R-parity and its consequences are used to
⁴⁵⁵ determine the physical motivation and search strategies for SUSY model at the LHC.

456 2.4. Experimental signatures of SUSY at the LHC

457 Should strongly interacting sparticles be within the experimental reach of the LHC, then
458 it is expected that they can be produced in a variety of ways.

- 459 • squark/anti-squark and gluino pairs can be produced via both gluon fusion and
460 quark/anti-quark scattering.
- 461 • a gluino and squark produced together via quark-gluon scattering
- 462 • squark pairs produced via quark-quark scattering

463 Whilst most SUSY searches invoke the requirement of R-parity to explore parameter
464 phase space, there still exist a whole plethora of possible SUSY model topologies which
465 could be discovered at the LHC.

466 During the 2011 run period at a $\sqrt{s} = 7$ TeV particular models were used to benchmark
467 performance and experimental reach of both CMS searches and previous experiments.
468 The Compressed Minimal SuperSymmetric Model (CMSSM) was initially chosen for a
469 number of reasons [38]. One of the most compelling being the reduction from the up to
470 105 new parameters introduced by SUSY in addition to the existing 19 of the SM to that
471 of just 5 free extra free parameters. It was this simplicity, combined with the theory not
472 requiring any fine tuning of particle masses to produce the experimentally verified SM
473 that made it an attractive model to interpret physics results.

474 However recent results from the LHC now strongly disfavour large swathes of CMSSM
475 parameter space [39][40][41]. In the face of such results a more pragmatic model indepen-
476 dent search strategy is now applied across most SUSY searches at the LHC, see Section
477 (2.4.1).

478 As previously stated, a stable LSP that exhibits the properties of a dark matter would
479 be weakly interacting and therefore will not be directly detected in a detector environment.
480 Additionally the cascade decays of supersymmetric particles to the LSP would also result
481 in significant hadronic activity. These signatures can then be characterised through
482 large amounts of hadronic jets (see Section (3.3.1)), leptons and a significant amount of
483 missing energy dependent upon the size of the mass splitting between the LSP and the
484 supersymmetric particle it has decayed from.

485 Whilst the SM contains processes which can exhibit a similar event topology to that
486 described above. The largest contribution of which comes in from the general QCD

487 environment of a hadron collider. A multitude of different analytical techniques are used
488 by experimental physicists to reduce or estimate any reducible or irreducible backgrounds,
489 allowing a possible **SUSY** signature to be extracted. The techniques employed within
490 this thesis are described in great detail within Section (4.1).

491 2.4.1. Simplified Models

492 With such a variety of different ways for a **SUSY** signal to manifest itself, it is necessary
493 to be able to interpret experimental reach through the masses of gluinos and squarks
494 which can excluded by experimental searches rather than on a model specific basis.

495 This is accomplished through **SMS** models, which are defined by a set of hypothetical
496 particles and a sequence of their production and decay [42][43]. In the **SMS** models
497 considered within this thesis, only the production process for the two primary particles
498 are considered. Each primary particle can undergo a direct or a cascade decay through
499 an intermediate new particle. At the end of each decay chain there remains a neutral,
500 undetected **LSP** particle, denoted $\tilde{\chi}_{LSP}$ which can represent a neutralino or gravitino.
501 Essentially it is easier to consider each **SMS** with branching ratios set to 100% The
502 masses of the primary particle and the **LSP** remain as free parameters, in which the
503 absolute value and relative difference between the primary and **LSP** particle alter the
504 kinematics of the event.

505 Different **SMS** models are denoted with a T-prefix, with a summary of the types
506 interpreted within this thesis listed below [44].

- 507 • **T1,T1xxxx**, models represent a simplified version of gluino pair production with
508 each gluino (superpartner to the gluon) undergoing a three-body decay to a quark-
509 antiquark pair and the **LSP** (i.e. $\tilde{g} \rightarrow q\bar{q}\tilde{\chi}_{LSP}$). The resultant final state from this
510 decay is typically 4 jets + \cancel{E}_T in the absence of initial/final state radiation and
511 detector effects. xxxx denotes models in which the quarks are of a specific flavour,
512 typically t or b quark-antiquarks.
- 513 • **T2,T2xx**, models represent a simplified version of squark anti-squark production
514 with each squark undergoing a two-body decay into a light-flavour quark and **LSP**
515 (i.e. $\tilde{q} \rightarrow q\tilde{\chi}_{LSP}$). This results in final states with less jets than gluino mediated
516 production, typically 2 jets + \cancel{E}_T when again ignoring the effect of initial/final state
517 radiation and detector effects. xx models again represent decays in which both the
518 quark and the squark within the decay is of a specific flavour, typically \tilde{t}/t or \tilde{b}/b .

Models rich in b and t quarks are interpreted within this thesis as they remain of particular interest within “Natural SUSY” scenarios [45][46]. The largest contribution to the quadratic divergence in the Higgs mass parameter comes from a loop of top quarks via the Yukawa coupling. Cancellation of these divergences can be achieved in supersymmetric theories by requiring a light right handed top squark, \tilde{t}_R , and left-handed double $SU(2)_L$ doublet containing top and bottom squarks, $(\tilde{\frac{t}{b}})_L$ [47].

These theories therefore solve the hierarchy problem by predicting light \sim EWK scale third generation sleptons, to be accessible at the LHC. Search strategies involving the requirement of b-tagging (see Section (3.3.2)) are used to give sensitivity to these type of SUSY scenarios and are discussed in greater detail within Chapter 5.

Two example decay chains are shown in Figure 2.2; the pair production of gluinos (T1) and the pair production of squarks (T2) decaying into SM particles and LSP’s.

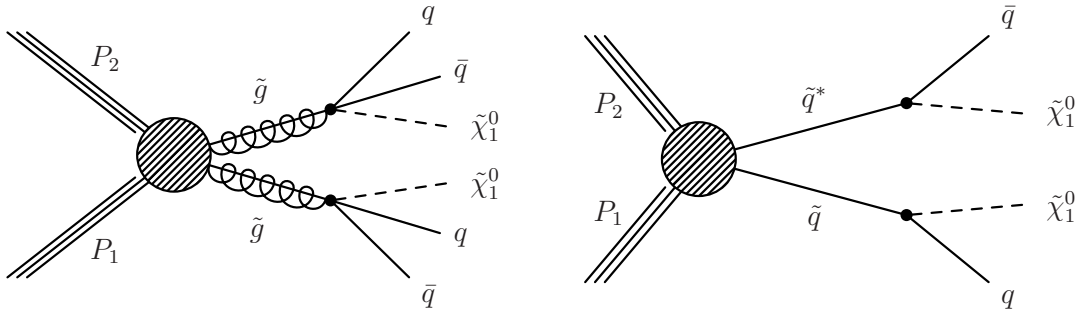


Figure 2.2.: Two example SMS model decays (T1 (left), T2 (right)), which are used in interpretations of physics reach by CMS.

Chapter 3.

⁵³¹ The LHC and the CMS Detector

⁵³² Probing the SM for signs of new physics would not be possible without the immensely
⁵³³ complex electronics and machinery that makes the TeV energy scale accessible for the
⁵³⁴ first time. This chapter will cover the LHC based at European Organization for Nuclear
⁵³⁵ Research (CERN) and the Compact Muon Solenoid (CMS) detector, being the experiment
⁵³⁶ the author is a member of. Section (3.2) serves to introduce an overview of the different
⁵³⁷ components of the CMS detector, with more detail spent on those that are relevant in
⁵³⁸ the search for Supersymmetric particles. Section (3.3) will focus on event and object
⁵³⁹ reconstruction again with more emphasis on jet level quantities which are most relevant
⁵⁴⁰ to the author's analysis research. Finally Section (3.4) will cover work performed by
⁵⁴¹ the author, as service to the CMS Collaboration, in measuring the performance of the
⁵⁴² Global Calorimeter Trigger (GCT) component of the L1 trigger during the 2012-2013
⁵⁴³ run period.

⁵⁴⁴ 3.1. The LHC

⁵⁴⁵ The LHC is a storage ring, accelerator, and collider of circulating beams of protons or
⁵⁴⁶ ions. Housed in the tunnel dug for the Large Electron-Positron collider (LEP), it is
⁵⁴⁷ approximately 27 km in circumference, 100 m underground, and straddles the border
⁵⁴⁸ between France and Switzerland outside of Geneva. It is currently the only collider
⁵⁴⁹ in operation that is able to study physics at the TeV scale. A double-ring circular
⁵⁵⁰ synchrotron, it was designed to collide both proton-proton (pp) and heavy ion (PbPb)
⁵⁵¹ with a centre of mass energy $\sqrt{s} = 14$ TeV at a final design luminosity of $10^{34}\text{cm}^{-2}\text{s}^{-1}$.

These counter-circulating beams of protons/Pb ions are merged in four sections around the ring to enable collisions of the beams, with each interaction point being home to one of the four major experiments; A Large Ion Collider Experiment (**ALICE**) [48], A Toroidal LHC ApparatuS (**ATLAS**) [49], Compact Muon Solenoid (**CMS**) [50] and Large Hadron Collider Beauty (**LHC-B**) [51] which record the resultant collisions. The layout of the **LHC** ring is shown in Figure 3.1. The remaining four sections contain acceleration, collimation and beam dump systems. In the eight arc sections, the beams are steered by magnetic fields of up to 8 T provided by super conduction dipole magnets, which are maintained at temperatures of 2 K using superfluid helium. Additional magnets for focusing and corrections are also present in straight sections within the arcs and near the interaction regions where the detectors are situated.

564

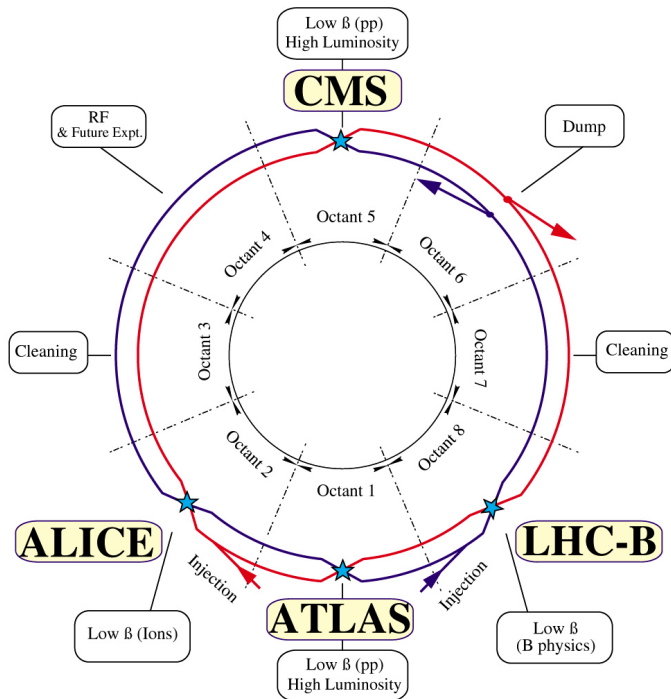


Figure 3.1.: A top down layout of the LHC. [52], with the position of the four main detectors labelled.

Proton beams are formed inside the Proton Synchrotron (**PS**) from bunches of protons 50 ns apart with an energy of 26 GeV. The protons are then accelerated in the Super Proton Synchrotron (**SPS**) to 450 GeV before being injected into the **LHC**. These **LHC** proton beams consists of many “bunches” i.e. approximately 1.1×10^{11} protons localized into less than 1 ns in the direction of motion. Before collision the beams are ramped to 4

570 TeV (2012) per beam in a process involving increasing the current passing through the
 571 dipole magnets. Once the desired \sqrt{s} energy is reached then the beams are allowed to
 572 collide at the interaction points. The luminosity falls regularly as the run progresses as
 573 protons are lost in collisions, and eventually the beam is dumped before repeating the
 574 process again.

575

576 Colliding the beams produced an instantaneous luminosity of approximately $5 \times$
 577 $10^{33} \text{ cm}^{-2}\text{s}^{-1}$ during the 2012 run. The high number of protons in each bunch increases
 578 the likelihood of multiple interactions with each crossing of the counter-circulating
 579 beams. This leads to isotropic energy depositions within the detectors positioned at these
 580 interaction points, increasing the energy scale of the underlying event. This is known as
 581 pile-up and the counteracting of it's effects are important to the many measurements
 582 performed at the LHC.

583 In the early phase of prolonged operation after the initial shutdown the machine
 584 operated in 2010-2011 at 3.5 TeV per beam, $\sqrt{s} = 7 \text{ TeV}$, delivering 6.13 fb^{-1} of data
 585 [53]. During the 2012-2013 run period, data was collected at an increased $\sqrt{s} = 8 \text{ TeV}$
 586 improving the sensitivity of searches for new physics. Over the whole run period 23.3
 587 fb^{-1} of data was delivered of which 21.8 fb^{-1} was recorded by the CMS detector as shown
 588 in Figure 3.2 [53]. A total of 12 fb^{-1} of 8 TeV certified data was collected by October
 589 2012, and it is this data which forms the basis of the results discussed within this thesis.

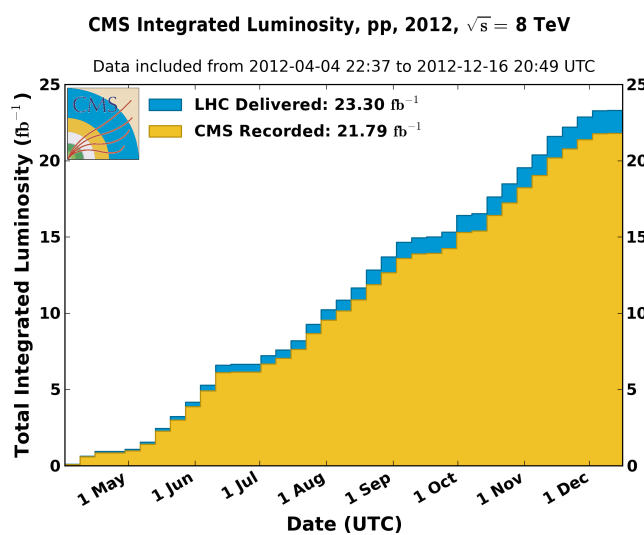


Figure 3.2.: The total integrated luminosity delivered to and collected by CMS during the 2012 8 TeV pp runs.

590 **3.2. The CMS detector**

591 The Compact Muon Solenoid (**CMS**) detector is one of two general purpose detectors
592 at the **LHC** designed to search for new physics. The detector is designed to provide
593 efficient identification and measurement of many physics objects including photons,
594 electrons, muons, taus, and hadronic showers over wide ranges of transverse momentum
595 and direction. Its nearly 4π coverage in solid angle allows for accurate measurement of
596 global transverse momentum imbalance. These design factors give **CMS** the ability to
597 search for direct production of **SUSY** particles at the TeV scale, making the search for
598 Supersymmetric particles one of the highest priorities among the wide range of physics
599 programmes at **CMS**.

600

601 **CMS** uses a right-handed Cartesian coordinate system with the origin at the interaction
602 point and the z-axis pointing along the beam axis, the x-axis points radially inwards to
603 the centre of the collider ring, with the y-axis points vertically upward. The azimuthal
604 angle, ϕ ranging between $[-\pi, \pi]$ is defined in the x-y plane starting from the x-axis. The
605 polar angle θ is measured from the z axis. The common convention in particle physics is
606 to express an out going particle in terms of ϕ and its pseudorapidity defined as

$$\eta = -\log \tan \left(\frac{\theta}{2} \right). \quad (3.1)$$

607 The variable $\Delta R = \sqrt{\Delta\phi^2 + \Delta\eta^2}$ is commonly used to define angular distance
608 between objects within the detector and additionally energy and momentum is typically
609 measured in the transverse plane perpendicular to the beam line. These values are
610 calculated from the x and y components of the object and are denoted as $E_T = E \sin \theta$
611 and $p_T = \sqrt{p_x^2 + p_y^2}$.

612 **3.2.1. Detector Subsystems**

613 As the range of particles produced in pp collisions interact in different ways with mat-
614 ter, **CMS** is divided into subdetector systems, which perform complementary roles to
615 identify the identity, mass and momentum of the different physics objects present in
616 each event. These detector sub-systems contained inside **CMS** are wrapped in layers

617 around a central 13 m long 4 T super conducting solenoid as shown in Figure 3.3. With
 618 the endcaps closed , CMS is a cylinder of length 22 m, diameter 15 m, and mass 12.5
 619 kilotons. A more detailed complete description of the detector can be found elsewhere [50].
 620

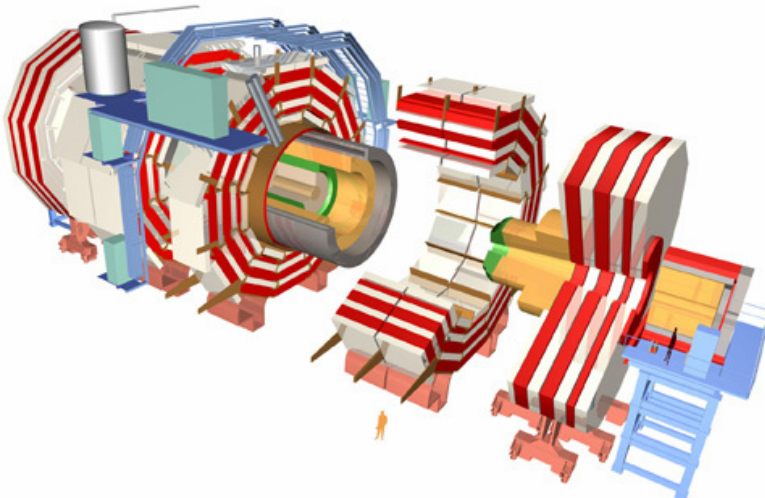


Figure 3.3.: A pictorial depiction of the CMS detector with the main detector subsystems labelled. [54]

621 3.2.2. Tracker

622 The inner-most subdetector of the barrel is the multi-layer silicon tracker, formed of a
 623 pixel detector component encased by layers of silicon strip detectors. The pixel detector
 624 consists of three layers of silicon pixel sensors providing measurements of the momentum,
 625 position coordinates of the charged particles as they pass, and the location of primary
 626 and secondary vertices between 4cm and 10cm transverse to the beam. Outside the pixel
 627 detector, ten cylindrical layers of silicon strip detectors extend the tracking system out to
 628 a radius of 1.20m from the beam line. The tracking system provides efficient and precise
 629 determination of the charges, momenta, and impact parameters of charged particles with
 630 the geometry of the tracker extending to cover a rapidity range up to $|\eta| < 2.5$.
 631

632 The tracking system also plays a crucial part in the identification of jets originating
 633 from b-quarks through measurement of displaced secondary vertices, which is covered in
 634 more detail in Section (3.3.2). The identification of b-jets is important in many searches

635 for natural SUSY models and forms an important part of the inclusive search strategy
636 described within Section (4.1.2).

637 **3.2.3. Electromagnetic Calorimeter**

638 Immediately outside of the tracker, but still within the magnet core, sits the Electromag-
639 netic CALorimeter (**ECAL**). Covering a pseudorapidity up to $|\eta| < 3$ and comprising
640 of over 75,000 PbWO₄ (lead tungstate) crystals that scintillate as particles deposit energy,
641 the **ECAL** provides high resolution measurements of the electromagnetic showers from
642 photons, electrons in the detector.

643

644 Lead tungstate is used because of its short radiation length ($X_0 \sim 0.9\text{cm}$) and small
645 Molieré radius ($\sim 2.1\text{cm}$) leading to high granularity and resolution. It's fast scintillation
646 time ($\sim 25\text{ns}$) reduces the effects of pile-up due to energy from previous collisions still
647 being read out, and its radiation hardness gives it longevity. The crystals are arranged
648 in modules which surround the beam line in a non-projective geometry, angled at 3°
649 with respect to the interaction point to minimise the risk of particles escaping down the
650 cracks between the crystals.

651

652 The **ECAL** is primarily composed of two sections, the Electromagnetic CALorime-
653 ter Barrel (**EB**) which extends in pseudo-rapidity to $|\eta| < 1.479$ with a crystal front
654 cross section of $22 \times 22 \text{ mm}^2$ and a length of 230 mm corresponding to 25.8 radia-
655 tion lengths, and the Electromagnetic CALorimeter Endcap (**EE**) covering a rapidity
656 range of $1.479 < |\eta| < 3.0$, which consists of two identical detectors on either side of
657 the **EB**. A lead-silicon sampling ‘pre-shower’ detector Electromagnetic CALorimeter
658 pre-Shower (**ES**) is placed before the endcaps to aid in the identification of neutral pions.
659 Their arrangement are shown in Figure 3.4.

660

661 Scintillation photons from the lead tungstate crystals are instrumented with Avalanche
662 Photo-Diodes (**APD**) and Vacuum Photo-Triodes (**VPT**) located in the **EB** and **EE**
663 respectively, converting the scintillating light into an electric signal which is consequently
664 used to determine the amount of energy deposited within the crystal . These instruments
665 are chosen for their resistance under operation to the strong magnetic field of **CMS**. The
666 scintillation of the **ECAL** crystals as well as the response of the **APDs** varies as a function

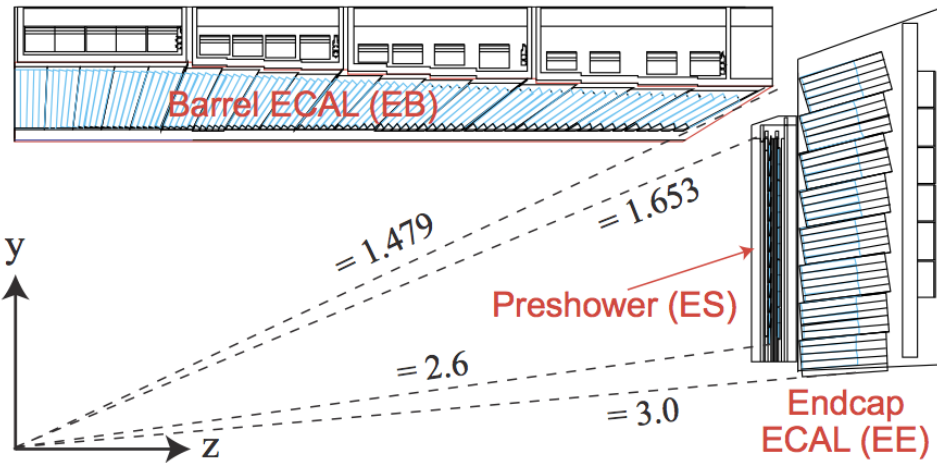


Figure 3.4.: Illustration of the CMS ECAL showing the arrangement of the lead tungstate crystals in the EB and EE. The ES is also shown and is located in front of the EE [55].

667 of temperature and so cooling systems continually maintain an overall constant ECAL
668 temperature $\pm 0.05^\circ\text{C}$.

669 3.2.4. Hadronic Calorimeter

670 Beyond the ECAL lies the Hadronic CALorimeter (HCAL) which is responsible for
671 the accurate measurement of hadronic showers, crucial for analyses involving jets or
672 missing energy signatures. The HCAL is a sampling calorimeter which consists of al-
673 ternating layers of brass absorber and plastic scintillator, except in the hadron forward
674 ($3.0 < |\eta| < 5.0$) region in which steel absorbers and quartz fibre scintillators are used
675 because of their increased radiation tolerance. Hadron showers are initiated in the
676 absorber layers inducing scintillation in the plastic scintillator tiles. These scintillation
677 photons are converted by wavelength shifting fibres for read-out by hybrid photodiodes.
678

679 The HCAL's size is constrained to a compact size by the presence of the solenoid,
680 requiring the placement of an additional outer calorimeter on the outside of the solenoid
681 to increase the sampling depth of the HCAL. A schematic of the HCAL can be seen in
682 Figure 3.5.
683

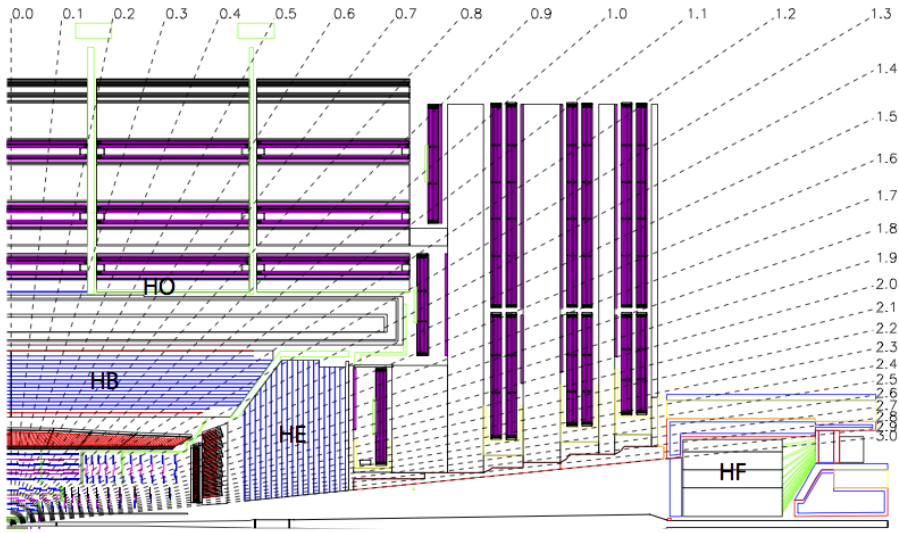


Figure 3.5.: Schematic of the hadron calorimeters in the r-z plane, showing the locations of the **HCAL** components and the **HF**. [50].

684 The **HCAL** covers the range $|\eta| < 5$ and consists of four subdetectors: the Hadron
 685 Barrel (**HB**) $|\eta| < 1.3$, the Hadron Outer (**HO**), the Hadron Endcaps (**HE**) $1.3 < |\eta| < 3.0$
 686 and the Hadron Forward (**HF**). The **HB** is contained between the outer edge of the
 687 **ECAL** and the inner edge of the solenoid, formed of 36 azimuthal wedges it is split
 688 between two half-barrel segments. The relatively short number of interaction lengths (λ_l ,
 689 the distance a hadron will travel through the absorber material before it has lost $\frac{1}{e}$ of
 690 its energy) within the **HB**, the lowest being $\lambda_l = 5.82$ for $|\eta| = 0$, facilitates the need
 691 for the ‘tail catching’ **HO** to increase the sampling depth in the central barrel rapidity
 692 region $|\eta| < 1.3$ to 11 interaction lengths . Significant fractions of the hadrons energy will
 693 be deposited in the **ECAL** as it passed through the detector. Therefore measurements
 694 of hadron energies in the central regions $|\eta| < 3.0$ use both the **ECAL** and **HCAL** to
 695 reconstruct the true energy from showering hadrons.

696 3.2.5. Muon Systems

697 Muons being too massive to radiate away energy via Bremsstrahlung, interact little in
 698 the calorimeters and mostly pass through the detector until they reach the system of
 699 muon detectors which forms the outer most part of the **CMS** detector.

700 Outside of the superconducting solenoid are four muon detection layers interleaved
701 with the iron return yokes which measure the muons energy via ionisation of gas within
702 detector elements. Three types of gaseous chamber are used. The Drift Tube (**DT**),
703 Cathode Stripe Chamber (**CSC**), and Resistive Plate Chamber (**RPC**) systems provide
704 efficient detection of muons with pseudo-rapidity $|\eta| < 2.4$. The best reconstruction
705 performance is obtained when the muon chamber is combined with the inner tracking
706 information to determine muon trajectories and their momenta [56].

707

708 **3.3. Event Reconstruction and Object Definition**

709 The goal of event reconstruction is to take the raw information recorded by the detector
710 and to compute from it higher-level quantities which can be used at an analysis level.
711 These typically correspond to an individual particle’s energy and momenta, or groups of
712 particles which shower in a narrow cone and the overall global energy and momentum
713 balance of the event. The reconstruction of these objects are described in great detail in
714 [57], however covered below are brief descriptions of those which are most relevant to the
715 analysis detailed in Section (4).

716 **3.3.1. Jets**

717 Quarks and gluons are produced copiously at the LHC in the hard scattering of partons.
718 As these quarks and gluons fragment, they hadronise and decay into a group of strongly
719 interactive particles and their decay products. These streams of particles travel in the
720 same direction, as they have been “boosted” by the momentum of the primary hadron.
721 These collections of decay products are reconstructed and identified together as a “jet”.

722 At **CMS** jets are reconstructed from energy deposits in the detector using the anti-kt
723 algorithm [58] with size parameter $\Delta R = 0.5$. The anti-kt jet algorithm clusters jets by
724 defining a distance between hard (high p_T) and soft (low p_T) particles such that soft
725 particles are preferentially clustered with hard particles before being clustered between
726 themselves. This produces jets which are robust to soft particle radiation from the pile-up
727 conditions experienced at the **LHC**.

728

729 There are two main type of jet reconstruction used at **CMS**, Calorimeter (Calo) and
730 Particle Flow (PF) jets [59]. Calorimeter jets are reconstructed using both the **ECAL**
731 and **HCAL** cells, combined into calorimeter towers . These calorimeter towers consist of
732 geometrically matched **HCAL** cells and **ECAL** crystals. Electronics noise is suppressed by
733 applying a threshold to the calorimeter cells, with pile-up effects reduced by a requirement
734 placed on the tower energy [60]. Calorimter jets are the jets used within the analyses
735 described in this thesis.

736 PF jets are formed from combining information from all of the **CMS** subdetectors
737 systems to determine which final state particles are present in the event. Generally,
738 any particle is expected to produce some combination of a track in the silicon tracker,
739 a deposit in the calorimeters, or a track in the muon system. The PF jet momentum
740 and spatial resolutions are greatly improved with respect to calorimeter jets, as the use
741 of the tracking detectors and of the high granularity of **ECAL** allows resolution and
742 measurement of charged hadrons and photons inside a jet, which together constitute \sim
743 85% of the jet energy [61].

744 The jets reconstructed by the clustering algorithm in **CMS** typically have an energy
745 that differs to the ‘true’ energy measured by a perfect detector. This stems from the
746 non-linear and nonuniform response of the calorimeters as well as other residual effects
747 including pile-up and underlying events, and therefore additional corrections are applied
748 to recover a uniform relative response as a function of pseudo-rapidity. These are applied
749 as separate sub corrections [62].

- 750 • A PU correction is first applied to the jet. It subtracts the average extra energy
751 deposited in the jet that comes from other vertices present in the event and is
752 therefore not part of the hard jet itself.
- 753 • p_T and η dependant corrections derived from Monte Carlo simulations are used to
754 account for the non-uniform response of the detector.
- 755 • p_T and η residual corrections are applied to data only to correct for difference
756 between data and Monte Carlo. The residual is derived from QCD dijet samples
757 and the p_T residual from $\gamma+$ jet and $Z+$ jets samples in data.

758 **3.3.2. B-tagging**

759 The decays of b quarks are suppressed by small CKM matrix elements. As a result, the
760 lifetimes of b-flavoured hadrons, produced in the fragmentation of b quarks, are relatively
761 long; \mathcal{O} 1ps. The identification of jets origination from b quarks is very important for
762 searches for new physics and for measurements of standard model processes.

763

764 Many different algorithms developed by CMS select b-quark jets based on variables
765 such as the impact parameters of the charged-particle tracks, the properties of recon-
766 structed decay vertices, and the presence or absence of a lepton, or combinations thereof.
767 One of the most efficient of which is the Combined Secondary Vertex (CSV) which
768 operates based on secondary vertex and track-based lifetime information, benchmarked
769 in ‘Loose’, ‘Medium’ and ‘Tight’ working points, of which the medium point is the tagger
770 used within the α_T search detailed in Section (4.1).

771 Using the CSV tagger, a likelihood-based discriminator distinguishes between jets
772 from b-quarks, and those from charm or light quarks and gluons, which is shown in Figure
773 3.6. The minimum thresholds on the discriminator for each working point correspond to
774 the misidentification probability for light-parton jets of 10%, 1%, and 0.1%, respectively,
775 in jets with an average p_T of about 80 GeV.

776 The b-tagging performance is evaluated to measure the b-jet tagging efficiency ϵ_b ,
777 and the misidentification probability of charm ϵ_c and light-parton jets ϵ_s . The tagging
778 efficiencies for each of these three jet flavours are compared between data and MC
779 simulation, from which a series of p_T and $|\eta|$ binned jet corrections are determined,

$$SF_{b,c,s} = \frac{\epsilon_{b,c,s}^{data}}{\epsilon_{b,c,s}^{MC}}. \quad (3.2)$$

780 These are collectively named ‘Btag Scale Factors’ and allow MC simulation to accu-
781 rately reflect the running conditions and performance of the tagging algorithm in data.
782 Understanding of the b-tagging efficiency is essential in order to minimise systematic
783 uncertainties in physics analyses that employ b-tagging.

784

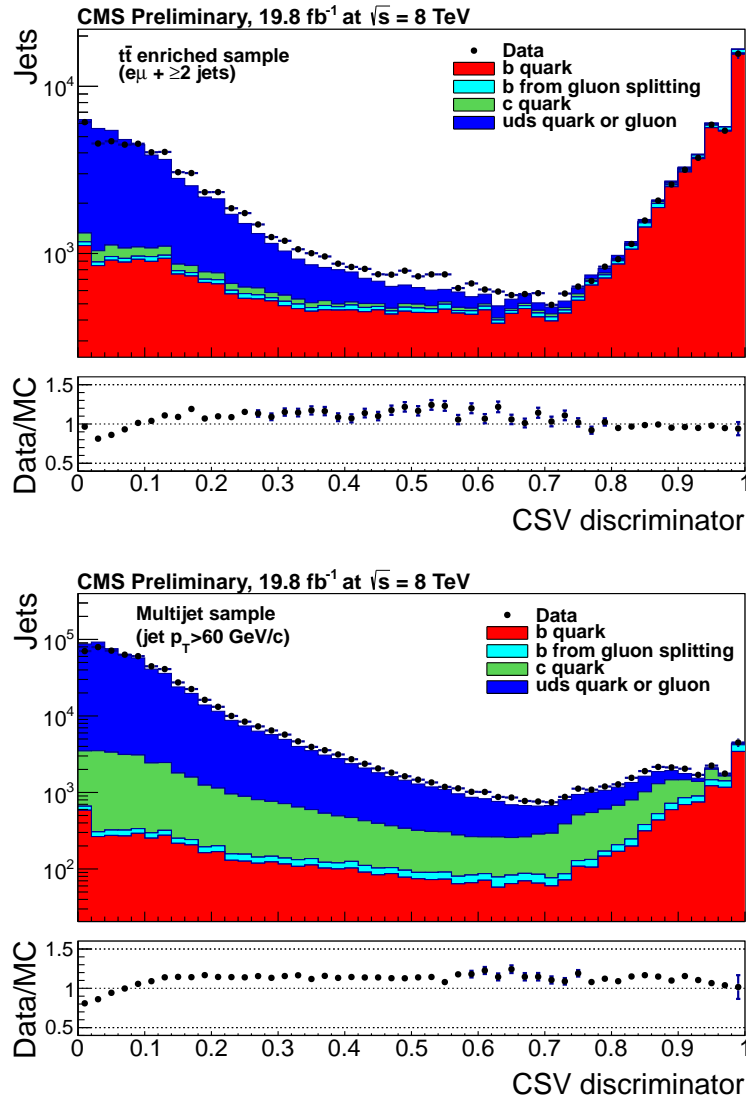


Figure 3.6.: CSV algorithm discriminator values in enriched $t\bar{t}$ bar (top) and inclusive multi jet samples (bottom) for b,c and light flavoured jets [63]. Working points are determined from the misidentification probability for light-parton jets to be tagged as a b-jet and are given as 0.244, 0.679 and 0.898 for L,M and T working points respectively.

785 The b-tagging efficiency is measured in data using several methods applied to multi
 786 jet events, primarily based on a sample of jets enriched in heavy flavour content. One
 787 method requires the collection of events with a soft muon within a cone $\Delta R < 0.4$ around
 788 the jet axis. Because the semileptonic branching fraction of b hadrons is significantly
 789 larger than that for other hadrons, these jets are more likely to arise from b quarks than
 790 from another flavour, with the resultant momentum component of the muon transverse
 791 to the jet axis larger for muons from b-hadron decays than from light or charm jets.

Additionally the performance of the tagger can also be benchmarked in $t\bar{t}$ events where in the SM, the top quark is expected to decay to a W boson and a b quark about 99.8% of the time [1]. Further selection criteria is applied to these events to further enrich the b quark content of these events. The methods to identify b-jets in data are discussed in great detail at [64]. The jet flavours are determined in simulation using truth level information and are compared to data to determine the correction scale factors (SF_b), which are displayed for the CSVM tagger in Figure 3.7.

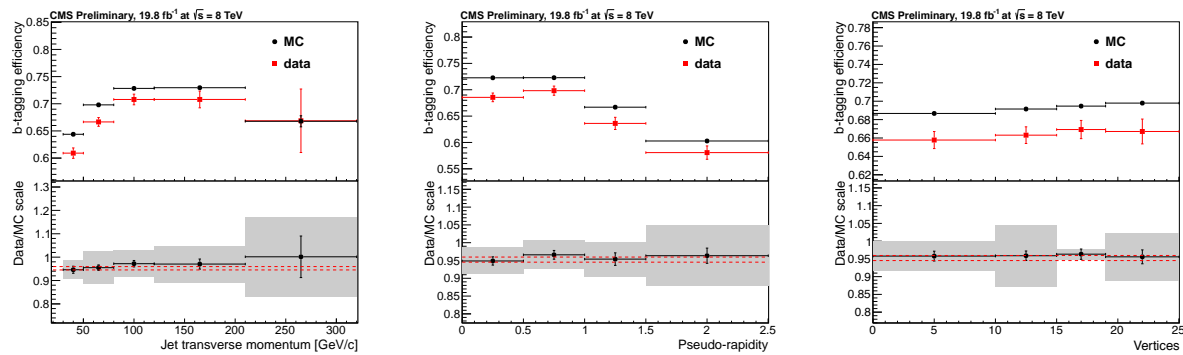


Figure 3.7.: Measured in $t\bar{t} \rightarrow$ di-lepton events using the CSVM tagger: (upper panels) b-tagging efficiencies and (lower panels) data/MC scale factor SF_b as a function of (left) jet p_T , (middle) jet $|\eta|$ and (right) number of primary vertices. In the lower panels, the grey filled areas represent the total statistical and systematic uncertainties, whereas the dotted lines are the average SF_b values within statistical uncertainties.

The measurement of the misidentification probability for light-parton jets relies on the inversion of tagging algorithms, selecting non-b jets using the same variables and techniques used in benchmarking the b-tagging efficiency. The scale factors (SF_s) to be applied to MC are shown in Figure 3.8 for the CSVM tagger.

3.4. Triggering System

With bunch crossings separated by just 25 ns, the rate at which data from all collisions would have to be written out and processed would be unfeasible. A two-tiered triggering system is applied at CMS in order to cope with the high collision rate of protons. The CMS trigger is designed to use limited information from each event to determine whether to record the event, reducing the rate of data taking to manageable levels whilst ensuring a high efficiency of interesting physics object events are selected.

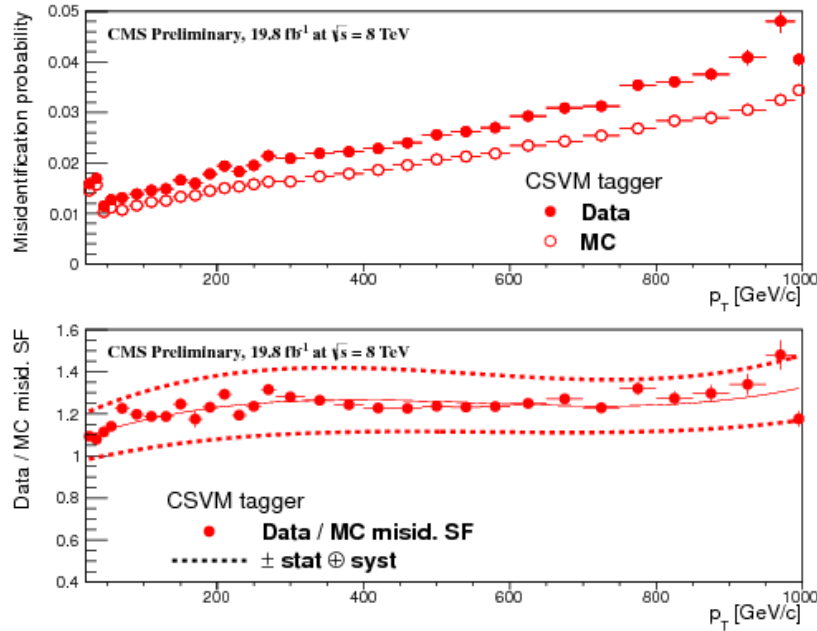


Figure 3.8.: For the **CSVM** tagging criterion: (top) misidentification probability in data (filled circles) and simulation (open circles); (bottom) scale factor for the misidentification probability. The last p_T bin in each plot includes all jets with $p_T > 1000$ GeV. The solid curve is the result of a polynomial fit to the data points. The dashed curves represent the overall statistical and systematic uncertainties on the measurements.

810 The **L1** is a pipelined, dead-timeless system based on custom-built electronics [65],
 811 and is a combination of several sub systems which is shown pictorially in Figure 3.9. The
 812 L1 system is covered in more detail within the following section along with a description
 813 of the service work undertaken by the author to benchmark the performance of the L1
 814 calorimeter trigger during the 2012 8 TeV run period.

815 The Higher Level Trigger (**HLT**) is a large farm of commercial computers [66]. The
 816 **HLT** processes events with software reconstruction algorithms that are more detailed,
 817 giving performance more similar to the reconstruction used offline. The **HLT** reduces
 818 the event rate written to disk by a factor of ~ 500 (~ 200 Hz). The recorded events are
 819 transferred from **CMS** to the **CERN** computing centre, where event reconstruction is
 820 performed, and then distributed to **CMS** computing sites around the globe for storage
 821 and analysis.

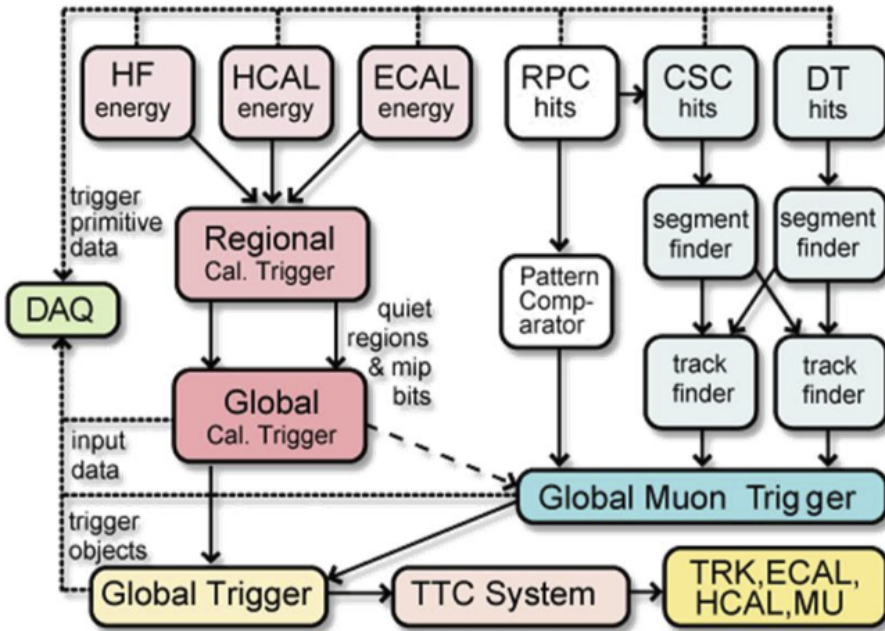


Figure 3.9.: The CMS L1 Trigger system.

3.4.1. The Level-1 Trigger

The L1 trigger reduces the rate of events collected from 40 MHz to ~ 100 kHz using information from the calorimeters and muon chambers, but not the tracker. A tree system of triggers is used to decide whether to pass on an event to the HLT for further reconstruction. Firstly the calorimeter and muon event information is kept separate, with local reconstruction of objects ($\mu, e, \gamma, \text{jets}$) performed by the Regional Calorimeter Trigger (RCT) and Regional Muon Trigger (RMT) respectively. The RCT generates up to 72 isolated and non-isolated electromagnetic objects. These are sorted by rank, which is equivalent to transverse energy E_T , with the four highest ranked electromagnetic objects being passed via the Global Calorimeter Trigger (GCT) and Global MuonTrigger (GMT) to the Global Trigger (GT).

In the L1 GCT, coarse measurements of the energy deposited in the electromagnetic and hadronic calorimeters are combined and by using sophisticated algorithms the following physics objects are formed:

- isolated and non-isolated electromagnetic objects (e and γ);
- hadronic jets in the central and forward sections of the hadronic calorimeters;

- 838 • hadronically decaying tau leptons;
- 839 • total transverse energy (E_T), the scalar sum of the energy measured at L1, and
840 missing transverse energy (\cancel{E}_T), defined as the vector sum of the energy of L1
841 objects;
- 842 • total transverse jet energy (H_T), the scalar sum of the energy of all L1 jet objects,
843 and missing transverse jet energy (\cancel{H}_T), defined as the vector sum of the energy of
844 L1 jets, are calculated from uncorrected L1 jets.

845 In addition quantities suitable for triggering minimum bias events, forward physics and
846 beam background events are calculated. Additionally relevant muon isolation information
847 is also passed on to the **GMT** for decisions involving the muon triggers where it is
848 combined with information from across the three muon sub-systems. The resultant final
849 accept/reject decision at **L1** is then performed by the **GT** based on the objects received
850 from the **GCT** and **GMT** (e/γ , μ , jets, E_T , \cancel{E}_T , H_T).

851 The L1 trigger is therefore of upmost importance to the functioning of the detector.
852 Without a high-performing trigger and a good understanding of it's performance, there
853 would be no data to analyse. Observations of how the L1 trigger performance is affected
854 by changing **LHC** running conditions over the 2012 run period and also the introduction
855 of a jet seed threshold to the L1 jet trigger algorithm is presented in the following Sections
856 (3.4.2 - 3.4.6).

857 3.4.2. L1 Trigger Jet Algorithm

858 The L1 jet trigger uses the transverse energy sums computed in the calorimeter (both
859 hadronic and electromagnetic) trigger regions. Each region consists of 4×4 trigger tower
860 windows, spanning a region of $\Delta\eta \times \Delta\phi = 0.087 \times 0.087$ in pseudorapidity-azimuth. The
861 jet trigger uses a 3×3 calorimeter region (112 trigger towers) sliding window technique
862 which spans the full (η, ϕ) coverage of the **CMS** calorimeter as shown in Figure 3.10.

863 In forming a L1 jet is it required that the central region to be higher than the eight
864 neighbouring regions $E_{T\text{central}} > E_{T\text{surround}}$. Additionally a minimum threshold of 5 GeV
865 on $E_{T\text{central}}$ was introduced during the 2012 run period to suppress noise from pile-up,
866 the effects of which are shown in Section (3.4.4).

867 The L1 jets are characterised by the E_T , summed over the 3×3 calorimeter regions,
868 which corresponds to 12×12 trigger towers in barrel and endcap or 3×3 larger **HF**

869 towers in the **HF**. The ϕ size of the jet window is the same everywhere, whilst the η
870 binning gets somewhat larger at high η due to calorimeter and trigger tower segmentation.
871 The jets are labelled by (η, ϕ) indexes of the central calorimeter region.

872 Jets with $|\eta| > 3.0$ are classified as forward jets, whereas those with $|\eta| < 3.0$ are
873 classified as central. The four highest energy central, forward and τ jets in the calorimeter
874 are passed through Look Up Table (**LUT**)'s, which apply a programmable η -dependent
875 jet energy scale correction. These are then used to make L1 trigger decisions.

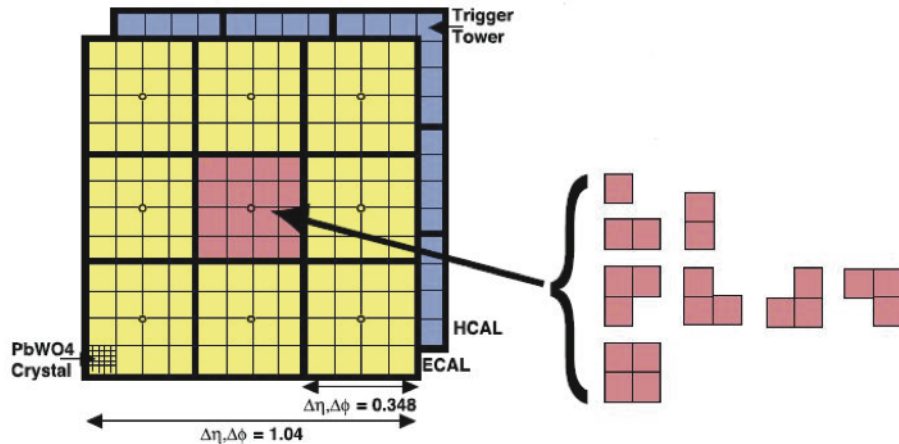


Figure 3.10.: Illustration of the Level-1 jet finding algorithm.

876 The performance of the L1 jets is evaluated with respect to offline jets, which are
877 taken from the standard Calo jet and the PF jet reconstruction algorithms of **CMS**.
878 Jets are corrected for pile-up and detector effects as described in [3.3.1](#). A moderate
879 level of noise rejection is applied to the offline jets by selecting jets passing the “loose
880 identification criteria for both Calo and PF. These criteria are summarised in Appendix
881 ([A.1](#)).

882 3.4.3. Measuring L1 Jet Trigger Efficiencies

883 The L1 jet efficiency is defined as the fraction of leading offline jets which were matched
884 with a L1 tau or central jet above a certain trigger threshold, divided by all the leading
885 offline jets in the event. This quantity is then plotted as a function of the offline jet E_T ,
886 η and ϕ .

887 The efficiency is determined by matching the L1 and reconstructed offline jets spatially
888 in $\eta - \phi$ space. This is done by calculating the minimum separation in ΔR between the

889 highest offline reconstructed jet in E_T ($E_T > 10$ GeV, $|\eta| < 3$) and any L1 jet. A jet will
 890 be matched if this value is found to be < 0.5 . Should more than one jet satisfy this, the
 891 jet closest in ΔR is taken as the matched jet. The matching efficiency is close to 100%,
 892 above ? 30(45) GeV for run 2012B(C) data (see Appendix (??)).

893 Each efficiency curve is fitted with a function which is the cumulative distribution
 894 function of an Exponentially Modified Gaussian (EMG) distribution:

$$895 \quad f(x; \mu, \sigma, \lambda) = \frac{\lambda}{2} \cdot e^{\frac{\lambda}{2}(2\mu + \lambda\sigma^2 - 2x)} \cdot \text{erfc}\left(\frac{\mu + \lambda\sigma^2 - x}{\sqrt{2}\sigma}\right) \quad (3.3)$$

where erfc is the complementary error function defined as:

$$\text{erfc}(x) = 1 - \text{erf}(x) = \frac{2}{\sqrt{\pi}} \int_x^\infty e^{-t^2} dt.$$

896 In this functional form, the parameter μ determines the point of 50% of the plateau
 897 efficiency and the σ gives the resolution. This parametrisation is used to benchmark
 898 the efficiency at the plateau, the turn-on points and resolution for each L1 Jet trigger.
 899 The choice of function is purely empirical. Previous studies used the error function
 900 alone, which described the data well at high threshold values but could not describe the
 901 efficiencies well at lower thresholds [67].

902 The efficiency turn-on curves for various L1 jet thresholds are evaluated as a function
 903 of the offline reconstructed jet E_T for central jets with $|\eta| < 3$. These are measured using
 904 single isolated μ triggers which have high statistics, and are orthogonal and therefore
 905 unbiased to the hadronic triggers under study. The efficiency is calculated with respect to
 906 offline Calo and PF Jets in Figure 3.11. Table 3.1 shows the values of these parameters,
 907 calculated for three example L1 single jet triggers taken from 2012 8 TeV data.

908 The results from the L1 single jet triggers shows good performance for both Calo and
 909 PF jets. A better resolution for Calo jets with respect to L1 jets quantities is observed.
 910 This effect is due to Calo jet reconstruction using the same detector systems as in L1 jets,
 911 whereas with PF jet construction using tracker and muon information, a more smeared
 912 resolution when compared to L1 is expected.

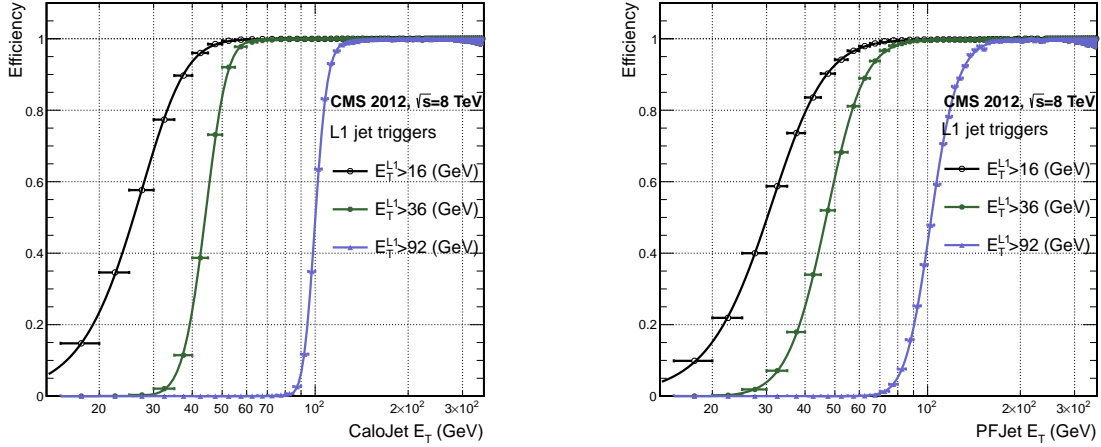


Figure 3.11.: L1 jet efficiency turn-on curves as a function of the offline CaloJet E_T (left) and PFJet E_T (right), measured in 2012 Run Period C data and collected with an isolated single μ data sample.

Trigger	Calo		PF	
	μ	σ	μ	σ
L1_SingleJet16	21.09 \pm 0.03	7.01 \pm 0.02	22.17 \pm 0.04	7.83 \pm 0.03
L1_SingleJet36	41.15 \pm 0.05	5.11 \pm 0.02	39.16 \pm 0.06	8.04 \pm 0.03
L1_SingleJet92	95.36 \pm 0.13	5.62 \pm 0.03	90.85 \pm 0.19	11.30 \pm 0.10

Table 3.1.: Results of a cumulative EMG function fit to the turn-on curves for L1 single jet triggers in run 2012 Run Period C, measured in an isolated μ data sample. The turn-on point, μ , and resolution, σ , of the L1 jet triggers are measured with respect to offline Calo Jets (left) and PF Jets (right).

3.4.4. Effects of the L1 Jet Seed

Between run period B and C of the 2012 data taking period, a jet seed threshold was introduced into the L1 trigger jet algorithm. There was previously no direct requirement made on the energy deposited in the central region. The introduction of a jet seed threshold required that the central region have $E_T \geq 5\text{GeV}$, and was introduced to counteract the effects of high pile up running conditions which create a large number of soft non-collimated jets, that are then added to the jets from the primary interaction or other soft jets from other secondary interactions [68]. This in turn causes a large increase in trigger rate due to the increase in the likelihood that the event causes the L1 trigger to fire. This was implemented to maintain trigger thresholds by cutting the rate of events recorded without significant reduction in the efficiency of physics events of interest.

The effect of the introduction of this jet seed threshold between these two run periods is benchmarked through a comparison of the efficiency of the L1 jet triggers with respect to offline Calo jets shown in Figure 3.12, and the L1 H_T trigger efficiency in Figure 3.14 which is compared to offline H_T constructed from Calo jets with $E_T \geq 40\text{GeV}$.

To negate any effects from different pile-up conditions in the run periods, the efficiencies are measured in events which contain between 15 and 20 primary vertices as defined in Appendix (A.2).

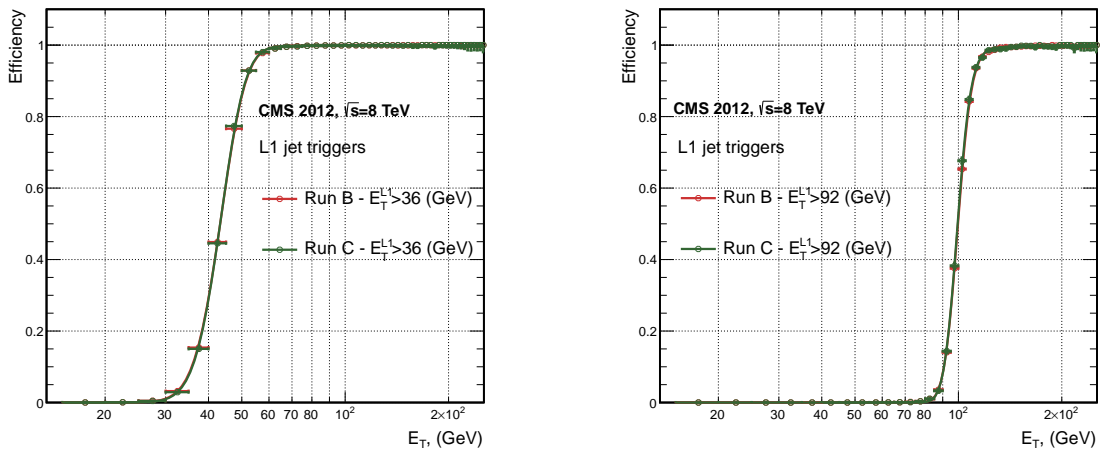


Figure 3.12.: L1 jet efficiency turn-on curves as a function of the offline CaloJet E_T , measured for the L1 SingleJet 36 and 92 trigger in 2012 run period B and C collected with an isolated single μ' sample.

It can be seen that the performance of the $E_T > 36, 92$ single jet are almost identical, with the jet seed having no measurable effect on these triggers as shown in Table 3.2 .

Trigger	2012B		2012C	
	μ	σ	μ	σ
L1_SingleJet36	40.29 ± 0.04	5.34 ± 0.02	40.29 ± 0.11	5.21 ± 0.05
L1_SingleJet92	94.99 ± 0.09	5.93 ± 0.06	94.82 ± 0.29	5.74 ± 0.18

Table 3.2.: Results of a cumulative EMG function fit to the turn-on curves for L1 single jet triggers in the 2012 run period B and C, preselected on an isolated muon trigger. The turn-on point μ and resolution σ of the L1 jet triggers are measured with respect to offline Calo Jets in run B (left) and run C (right).

For the H_T triggers, a large increase in rate during high pile-up conditions is expected. This is due to the low energy threshold required for a jet to be added to the L1 H_T sum,

which is compiled from all uncorrected L1 jets formed in the RCT. The introduction of the jet seed threshold removes the creation of many of these soft low E_T jets, thus lowering the H_T calculation at L1. The effect on the trigger cross section for L1 H_T 150 trigger can be seen in Figure 3.13.

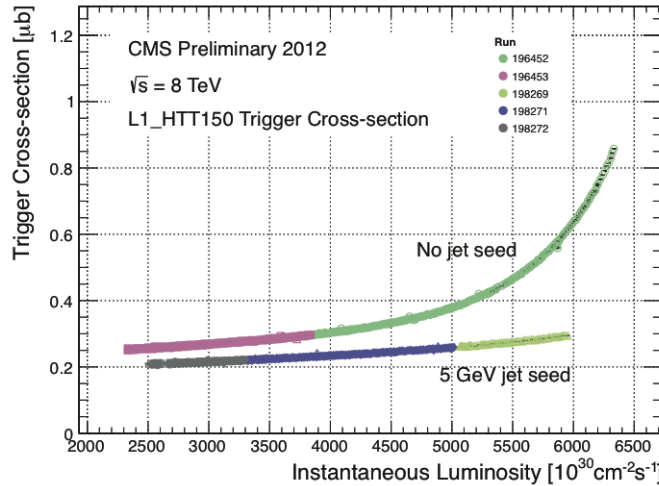


Figure 3.13.: Trigger cross section for the L1HTT150 trigger path. Showing that a 5 GeV jet seed threshold dramatically reduces the dependance of cross section on the instantaneous luminosity for L1 H_T triggers [69].

Different behaviours for the trigger turn ons between these run periods are therefore expected. The turn on point is observed to shift to higher H_T values after the introduction of the jet seed threshold, whilst having a sharper resolution due to less pile-up jets being included the H_T sum, the results are shown in Table 3.3.

Trigger	2012B		2012C	
	μ	σ	μ	σ
L1 HT-100	157.5 ± 0.08	32.9 ± 0.08	169.8 ± 0.08	28.7 ± 0.03
L1 H1-150	230.9 ± 0.02	37.3 ± 0.01	246.4 ± 0.16	31.8 ± 0.05

Table 3.3.: Results of a cumulative EMG function fit to the turn-on curves for H_T in run 2012 B and C, preselected on an isolated single μ trigger. The turn-on point μ , resolution σ of the L1 H_T triggers are measured with respect to offline H_T formed from CaloJets with a $E_T \geq 40$ in run period B (left) and C (right).

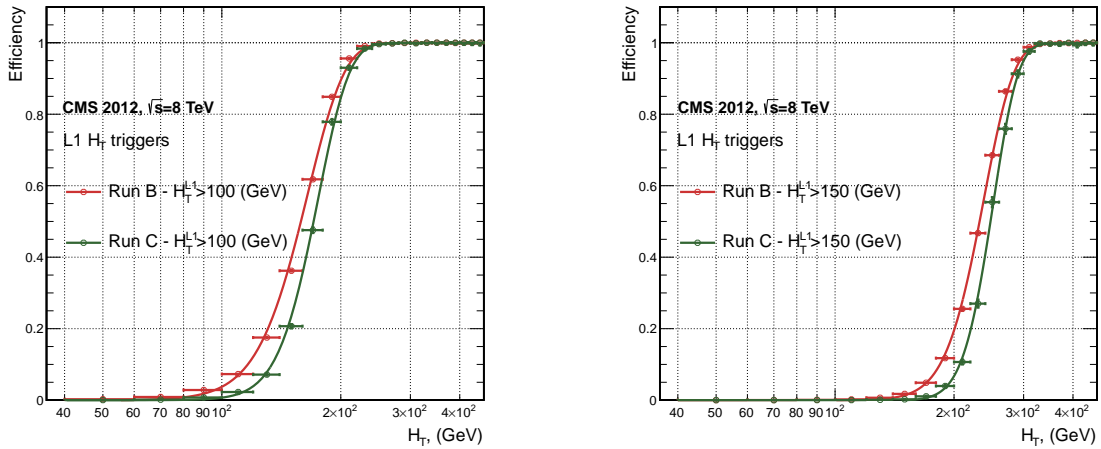


Figure 3.14.: L1 H_T efficiency turn-on curves as a function of the offline CaloJet H_T , measured for the L1 H_T 100 and 150 trigger during the run 2012 B and C collected using an isolated single μ triggered sample.

943 3.4.5. Robustness of L1 Jet Performance against Pile-up

944 The performance of the L1 single jet triggers is evaluated in different pile-up conditions
 945 to benchmark any dependence on pile-up. Three different pile-up bins of 0-10, 10-20 and
 946 >20 vertices are defined, reflecting the low, medium and high pile-up running conditions
 947 at CMS in 2012. This is benchmarked relative to Calo and PF jets for the run 2012 C
 948 period where the jet seed threshold is applied, with L1 single jet thresholds of 16, 36 and
 949 92 GeV, shown in Figure 3.15. The results of fits to these efficiency turn-on curves are
 950 given in Table 3.4 and Table 3.5 for Calo and PF jets respectively.

Vertices	0-10		11-20		> 20	
	μ	σ	μ	σ	μ	σ
L1_SingleJet16	19.9 ± 0.1	6.1 ± 0.3	20.8 ± 0.1	6.5 ± 0.1	22.3 ± 0.2	7.5 ± 0.1
L1_SingleJet36	41.8 ± 0.1	4.6 ± 0.1	40.9 ± 0.1	5.1 ± 0.1	40.6 ± 0.6	5.9 ± 0.2
L1_SingleJet92	95.9 ± 0.2	5.4 ± 0.1	95.2 ± 0.2	5.6 ± 0.1	94.5 ± 0.6	6.2 ± 0.3

Table 3.4.: Results of a cumulative EMG function fit to the efficiency turn-on curves for L1 single jet triggers in the 2012 run period C, measured from isolated μ triggered data. The turn-on point, μ , and resolution, σ , of the L1 jet triggers are measured with respect to offline Calo jets in low (left), medium (middle) and high (right) pile-up conditions.

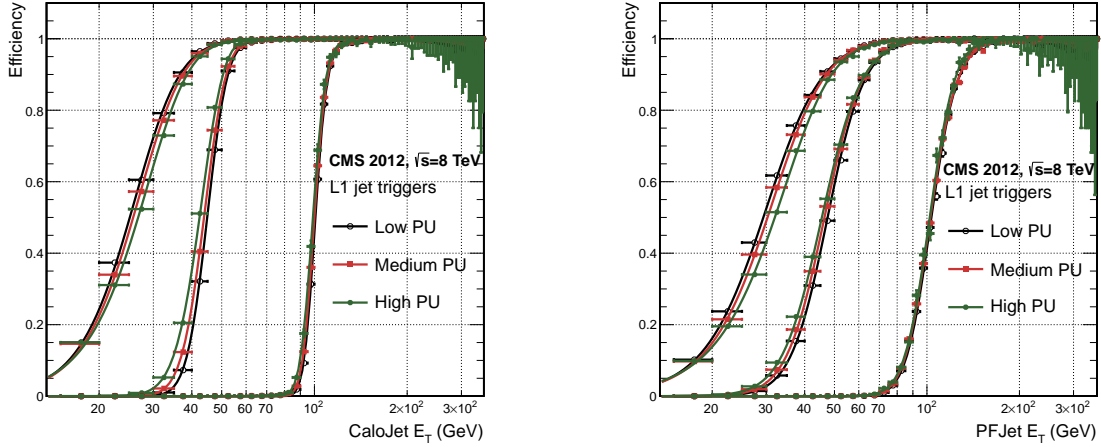


Figure 3.15.: L1 jet efficiency turn-on curves as a function of the leading offline E_T Calo (left) and PF (right) jet, for low, medium and high pile-up conditions.

Vertices	0-10		11-20		> 20	
	μ	σ	μ	σ	μ	σ
L1_SingleJet16	21.1 ± 0.1	7.16 ± 0.05	22.34 ± 0.1	7.9 ± 0.1	24.6 ± 0.2	9.5 ± 0.1
L1_SingleJet36	39.6 ± 0.1	7.4 ± 0.1	38.4 ± 0.1	7.4 ± 0.1	37.1 ± 0.2	7.5 ± 0.1
L1_SingleJet92	91.6 ± 0.3	11.3 ± 0.2	90.4 ± 0.3	11.2 ± 0.1	92.0 ± 0.9	12.1 ± 0.4

Table 3.5.: Results of a cumulative EMG function fit to the efficiency turn-on curves for Level-1 single jet triggers in the 2012 run period C, measured from isolated μ triggered data. The turn-on point, μ , and resolution, σ , of the L1 jet triggers are measured with respect to offline PF jets in low (left), medium (middle) and high (right) pile-up conditions.

951 No significant drop in efficiency is observed in the presence of a high number of
 952 primary vertices. The increase in hadronic activity in higher pile-up conditions, combined
 953 with the absence of pile-up subtraction for L1 jets, results in the expected observation of
 954 a decrease in the μ value of the efficiency turn-ons as a function of pile-up, while the
 955 resolution, σ of the turn-ons are found to gradually worsen as expected with increasing
 956 pile-up.

957 These features are further emphasised when shown as a function of

$$\frac{(L1 E_T - \text{Offline } E_T)}{\text{Offline } E_T} \quad (3.4)$$

in bins of matched leading offline jet E_T , of which the individual fits can be found in Appendix (B.2). Each of these distributions are fitted with an EMG function as defined in Equation (3.3).

The μ , σ and λ values extracted for the low, medium and high pile-up conditions are shown for Calo and PF jets in Figure 3.16 and Figure 3.17 respectively. The central value of $\frac{(L1 E_T - \text{Offline } E_T)}{\text{Offline } E_T}$ is observed to increases as a function of jet E_T , whilst the resolution is also observed to improve at higher offline jet E_T .

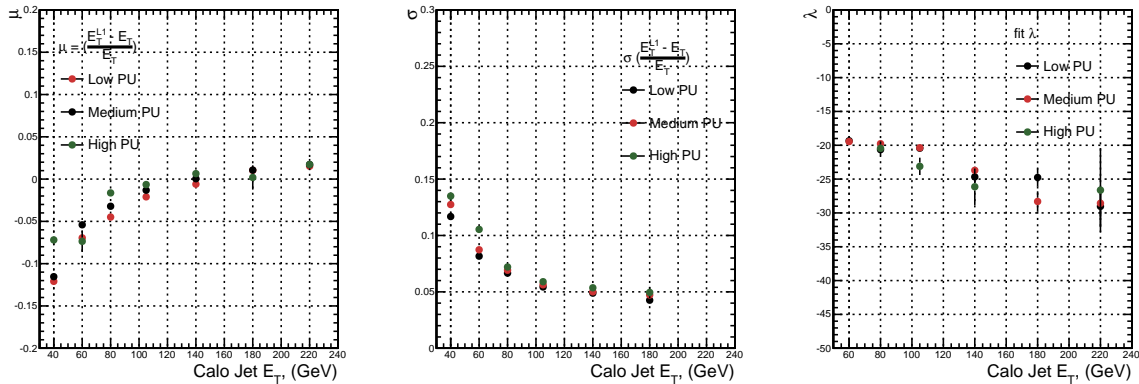


Figure 3.16.: Fit values from an EMG function fitted to the resolution plots of leading Calo jet E_T measured as a function of $\frac{(L1 E_T - \text{Offline } E_T)}{\text{Offline } E_T}$ for low, medium and high pile-up conditions. The plots show the mean μ (left), resolution σ (middle) of the Gaussian as well as the decay term λ (right) of the exponential.

The resolution of other L1 energy sum quantities, H_T , \not{E}_T and $\sum E_T$ parameterised as in Equation (3.4), can be found in Appendix (B.3). The same behaviour observed for the single jet triggers is also found for these quantities, where in the presence of higher pile-up the μ values are shifted to higher values, with a worsening resolution, σ again due to the increase in soft pile-up jets and the absence of pile-up subtraction at L1.

3.4.6. Summary

The performance of the CMS Level-1 Trigger has been studied and evaluated for jets and energy sum quantities using data collected during the 2012 LHC 8TeV run. These studies include the effect of introduction of a 5 GeV jet seed threshold into the jet algorithm configuration, the purpose of which is to mitigate the effects of pile-up on the rate of L1 triggers whilst not adversely affecting the efficiency of these triggers. No significant

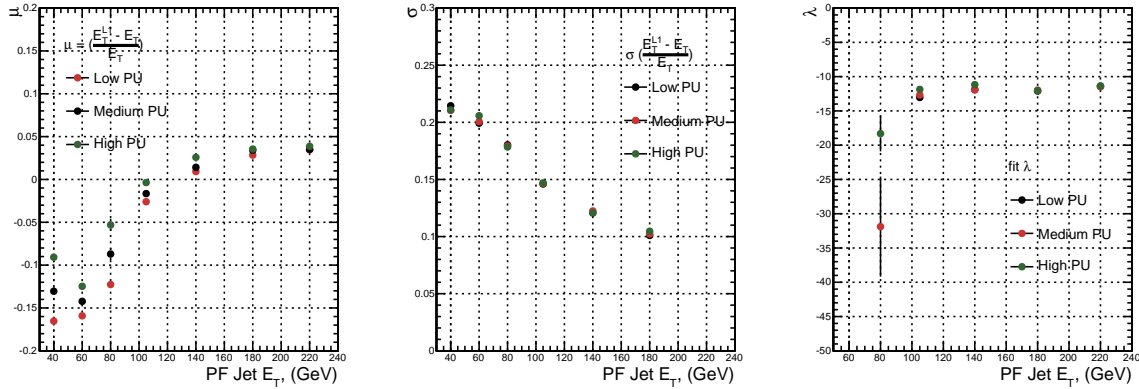


Figure 3.17.: Fit values from an **EMG** function fitted to the resolution plots of leading PF jet E_T measured as a function of $\frac{(L1\ E_T - \text{Offline}\ E_T)}{\text{Offline}\ E_T}$ for low and medium pile-up conditions. The plots show the mean μ (left), resolution σ (middle) of the Gaussian as well as the decay term λ (right) of the exponential.

976 change in performance is observed with this change and good performance is observed
 977 for a range of L1 quantities.

Chapter 4.

978 SUSY searches in Hadronic Final 979 States

980 In this chapter a model independent search for **SUSY** in hadronic final states with \cancel{E}_T
981 using the α_T variable and b-quark multiplicity is introduced and described in detail. The
982 results presented are based on a data sample of pp collisions collected in 2012 at $\sqrt{s} = 8$
983 TeV, corresponding to an integrate luminosity of $11.7 \pm 0.5 \text{ fb}^{-1}$.

984 The kinematic variable α_T is motivated as a variable to provide strong rejections
985 of QCD backgrounds, whilst maintaining sensitivity to possible a **SUSY** signal within
986 Section (4.1). The search and trigger strategy in addition to the event reconstruction
987 and selection are outlined within Sections (4.1.2-4.1.4).

988 The method in which the **SM** background is estimated using an analytical technique
989 to improve statistical precision at higher b-tag multiplicities is detailed within Section
990 (4.1.5), with a discussion on the impact of b-tagging and mis-tagging scale factors between
991 data and MC on any background predictions. Finally a description of the formulation of
992 appropriate systematic uncertainties applied to the background predictions to account for
993 theoretical uncertainties and limitations in the simulation modelling of event kinematics
994 and instrumental effects is covered in Section (4.1.6).

995 In addition to the α_T search, a complimentary technique is discussed as a means to
996 predict the distribution of 3 and 4 reconstructed b-quark jets in an event in Section
997 (4.2). The recent discovery of the Higgs boson has made third-generation “Natural **SUSY**”
998 models attractive, given that light top and bottom squarks are a candidate to stabilise
999 divergent loop corrections to the Higgs boson mass.

1000 Using the α_T search as a base, a simple templated fit is employed to estimate the
 1001 **SM** background in higher b-tag multiplicities (3-4) from a region of a low number
 1002 of reconstructed b-jets (0-2). The predictions using this technique are first tested in
 1003 simulation before being compared to the **SM** background predictions obtained from the
 1004 α_T search.

1005 The experimental reach of the analysis discussed within this thesis is interpreted in
 1006 two classes of **SMS** models, the topologies of which are detailed in Section (2.4.1). The
 1007 **SMS** models considered in this analysis are summaries in Table 4.1. For each model, the
 1008 **LSP** is assumed to be the lightest neutralino.

1009 Within Table 4.1 is also defined reference points, parameterised in terms of parent
 1010 gluino/squark and **LSP** sparticle masses, m_{parent} and m_{LSP} , respectively, which are used
 1011 within the following two chapters to demonstrate potential yields within the signal region
 1012 of the search. The masses are chosen to reflect parameter space which is within the
 1013 expect sensitivity reach of the search.

Model	Production/decay mode	Reference model	
		m_{parent}	m_{LSP}
G1 (T1)	$pp \rightarrow \tilde{g}\tilde{g}^* \rightarrow q\bar{q}\tilde{\chi}_1^0 q\bar{q}\tilde{\chi}_1^0$	700	300
G2 (T1bb)	$pp \rightarrow \tilde{g}\tilde{g}^* \rightarrow b\bar{b}\tilde{\chi}_1^0 b\bar{b}\tilde{\chi}_1^0$	900	500
G3 (T1tt)	$pp \rightarrow \tilde{g}\tilde{g}^* \rightarrow t\bar{t}\tilde{\chi}_1^0 t\bar{t}\tilde{\chi}_1^0$	850	250
D1 (T2)	$pp \rightarrow \tilde{q}\tilde{q}^* \rightarrow q\tilde{\chi}_1^0 \bar{q}\tilde{\chi}_1^0$	600	250
D2 (T2bb)	$pp \rightarrow \tilde{b}\tilde{b}^* \rightarrow b\tilde{\chi}_1^0 \bar{b}\tilde{\chi}_1^0$	500	150
D3 (T2tt)	$pp \rightarrow \tilde{t}\tilde{t}^* \rightarrow t\tilde{\chi}_1^0 \bar{t}\tilde{\chi}_1^0$	400	0

Table 4.1.: A summary of the **SMS** models interpreted in this analysis, involving both direct (D) and gluino-induced (G) production of squarks and their decays. Reference models are also defined in terms of parent and **LSP** sparticle mass

1014 4.1. The α_T search

1015 The experimental signature of **SUSY** signal in the hadronic channel would manifest as a
 1016 final state containing energetic jets and \cancel{E}_T . The search focuses on topologies where new
 1017 heavy supersymmetric, R-parity conserving particles are pair-produced in pp collisions.
 1018 These particles decaying to a **LSP** escape the detector undetected, leading to significant
 1019 missing energy and missing hadronic transverse energy,

$$\mathcal{H}_T = \left| \sum_{i=1}^n p_T^{jet_i} \right|, \quad (4.1)$$

1020 defined as the vector sum of the transverse energies of jets selected in an event.
1021 Energetic jets produced in the decay of these supersymmetric particles also can produce
1022 significant visible transverse energy,

$$H_T = \sum_{i=1}^n E_T^{jet_i}, \quad (4.2)$$

1023 defined as the scalar sum of the transverse energies of jets selected in an event.

1024 A search within this channel is greatly complicated in a hadron collider environment,
1025 where the overwhelming background comes from inherently balanced multi-jet (“QCD”)
1026 events which are produced with an extremely large cross section as demonstrated within
1027 Figure 4.1. \cancel{E}_T can appear in such events with a substantial mis-measurement of jet
1028 energy or missed objects due to detector miscalibration or noise effects.

1029 Additional SM background from EWK processes with genuine \cancel{E}_T from escaping
1030 neutrinos comprise the irreducible background within this search and come mainly from:

- 1031 • $Z \rightarrow \nu\bar{\nu}$ + jets,
- 1032 • $W \rightarrow l\nu$ + jets,
- 1033 • $t\bar{t}$ with at least one leptonic W decay.

1034 The search is designed to have a strong separation between events with genuine and
1035 “fake” \cancel{E}_T which is achieved primarily through the dimensionless kinematic variable, α_T
1036 [70][71].

1037 4.1.1. The α_T variable

1038 For a perfectly measured di-jet QCD event, conservation laws dictate that they must be
1039 produced back-to-back and of equal magnitude. However in di-jet events with real \cancel{E}_T ,
1040 both of these jets are produced independently of one another, depicted in Figure 4.2.

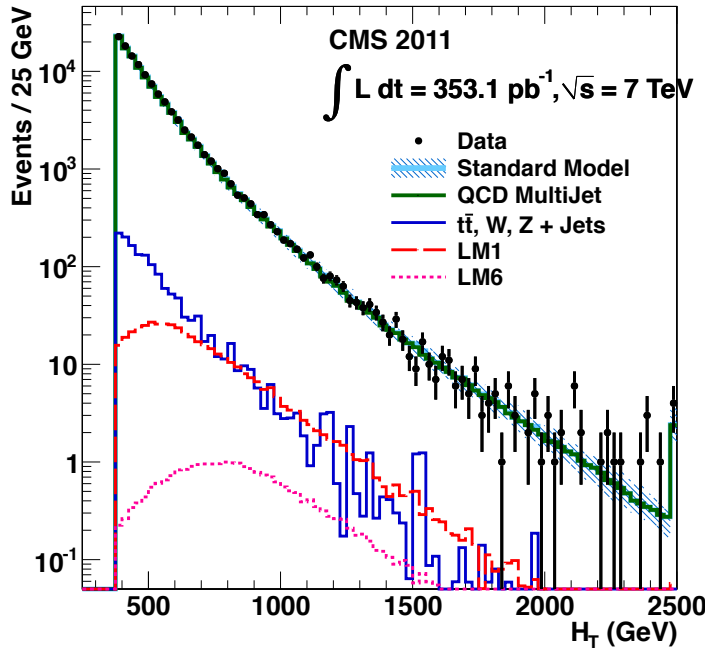


Figure 4.1.: Reconstructed offline H_T for 11.7fb^{-1} of data after a basic pre-selection. Sample is collected from prescaled H_T triggers. Overlaid are expectations from MC simulation of EWK processes as well as a reference signal model (labelled D2 from Table 4.1).

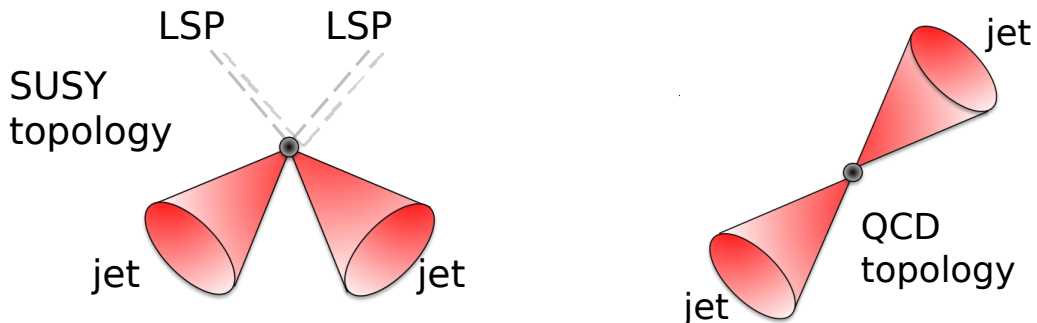


Figure 4.2.: The event topologies of background QCD dijet events (right) and a generic SUSY signature with genuine \cancel{E}_T (left).

Exploiting this feature leads to the formulation of α_T in di-jet systems defined as,

$$\alpha_T = \frac{E_T^{j2}}{M_T}, \quad (4.3)$$

1042 where E_T^{j2} is the transverse energy of the least energetic of the two jets and M_T
1043 defined as:

$$M_T = \sqrt{\left(\sum_{i=1}^2 E_T^{j_i}\right)^2 - \left(\sum_{i=1}^2 p_x^{j_i}\right)^2 - \left(\sum_{i=1}^2 p_y^{j_i}\right)^2} \equiv \sqrt{H_T^2 - \mathcal{H}_T^2}. \quad (4.4)$$

1044 A perfectly balanced di-jet event i.e. $E_T^{j_1} = E_T^{j_2}$ would give an $\alpha_T = 0.5$, where as
1045 events with jets which are not back-to-back, for example in events in which a W or Z
1046 recoils off a system of jets, α_T can achieve values in excess of 0.5.

1047 α_T can be extended to apply to any arbitrary number of jets, undertaken by modelling
1048 a system of n jets as a di-jet system, through the formation of two pseudo-jets [72].
1049 The two pseudo-jets are built by merging the jets present in the event such that the
1050 2 pseudo-jets are chosen to be as balanced as possible, i.e the $\Delta H_T \equiv |E_T^{pj_1} - E_T^{pj_2}|$ is
1051 minimised between the two pseudo jets. Using Equation (4.4), α_T can be rewritten as,

$$\alpha_T = \frac{1}{2} \frac{H_T - \Delta H_T}{\sqrt{H_T^2 - \mathcal{H}_T^2}} = \frac{1}{2} \frac{1 - \Delta H_T/H_T}{\sqrt{1 - (\mathcal{H}_T/H_T)^2}}. \quad (4.5)$$

1052 The distribution of α_T for the two jet categories used within this analysis, 2,3 and
1053 ≥ 4 jets, is shown in the Figure.4.3, demonstrating the ability of the α_T variable to
1054 discriminate between multi jet events and EWK processes with genuine E_T in the final
1055 state.

1056 The α_T requirement used within the search is chosen to be $\alpha_T > 0.55$ to ensure
1057 that the QCD multijet background is negligible even in the presence of moderate jet
1058 mis-measurement. There still remains other effects which can cause multijet events to
1059 artificially have a large α_T value, which are discussed in detail in Section (4.1.4).

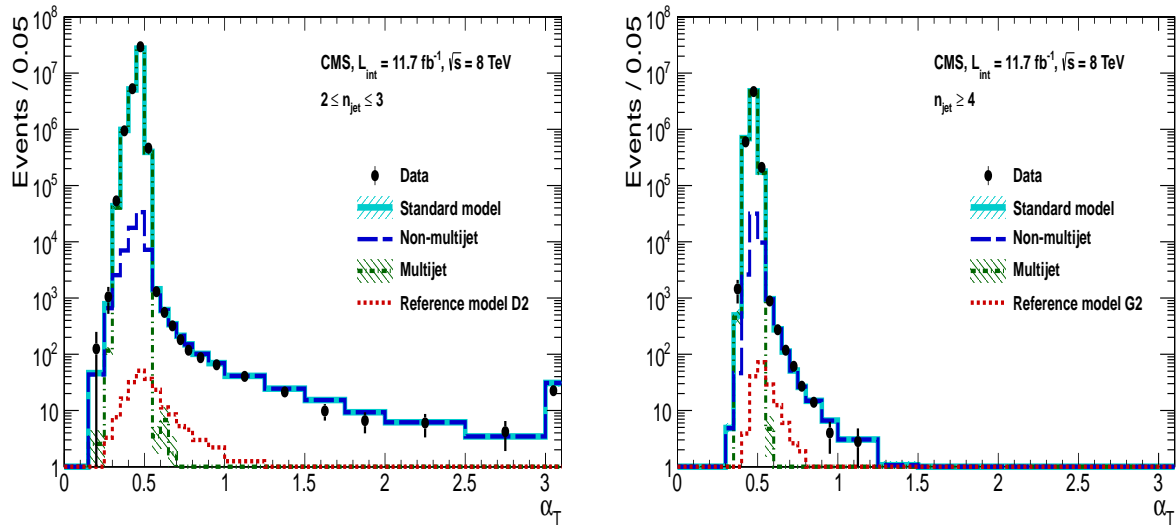


Figure 4.3.: The α_T distributions for the low 2-3 (left) and high ≥ 4 (right) jet multiplicities after a full analysis selection and shown for $H_T > 375$. Data is collected using both prescaled H_T triggers and dedicated α_T triggers for below and above $\alpha_T = 0.55$ respectively. . Expected yields as given by simulation are also shown for multijet events (green dash-dotted line), EWK backgrounds with genuine \cancel{E}_T (blue long-dashed line), the sum of all SM processes (cyan solid line) and the reference signal model D2 (left, red dotted line) or G2 (right, red dotted line).

1060 4.1.2. Search Strategy

1061 4.1.3. Trigger Strategy

1062 4.1.4. Event Selection

1063 4.1.5. Background Estimation

1064 4.1.6. Systematic Uncertainties on Transfer Factors

1065 4.2. Searches for Natural SUSY with B-tag templates.

1067 Btag Templates blah blah

Chapter 5.

¹⁰⁶⁸ Results

¹⁰⁶⁹ Results at 12fb 8TeV

¹⁰⁷⁰ 5.1. Statistical Interpretation

¹⁰⁷¹ Likelihood stuff

¹⁰⁷² 5.2. Interpretation in Simplified Signal Models

¹⁰⁷³ Result interpretation

¹⁰⁷⁴

Appendix A.

¹⁰⁷⁵ Miscellaneous

¹⁰⁷⁶ A.1. Noise Filters

¹⁰⁷⁷ For Calo jets the following criteria were applied:

¹⁰⁷⁸ • N90 hits > 1 ,

¹⁰⁷⁹ • HBHE > 0.01 ,

¹⁰⁸⁰ • fHPD < 0.98 ,

¹⁰⁸¹ For PF jets the following criteria were applied:

¹⁰⁸² • Neutral hadron fraction < 0.99 ,

¹⁰⁸³ • Neutral EM fraction < 0.99 ,

¹⁰⁸⁴ • Number of constituents > 1 ,

¹⁰⁸⁵ • Charged hadron fraction > 0 ,

¹⁰⁸⁶ • Charged multiplicity > 0 ,

¹⁰⁸⁷ • Charged EM fraction < 0.99 .

¹⁰⁸⁸ The following noise filters are applied, to remove events with spurious, non-physical
¹⁰⁸⁹ jets or missing transverse energy.

¹⁰⁹⁰ • CSC tight beam halo filter,

¹⁰⁹¹ • HBHE noise filter with isolated noise rejection,

- 1092 • HCAL laser filter,
- 1093 • ECAL dead cell trigger primitive (TP) filter,
- 1094 • Tracking failure filter,
- 1095 • Bad EE Supercrystal filter,
- 1096 • ECAL Laser correction filter.

1097 A.2. Primary Vertices

1098 The pileup per event is defined by the number of 'good' reconstructed primary vertices
1099 in the event, with each vertex satisfying the following requirements

- 1100 • $N_{dof} > 4$;
- 1101 • vertex position along the bead direction of $|z_{vtx}| < 24\text{cm}$;
- 1102 • vertex position perpendicular to the beam of $\rho < 2\text{cm}$.

Appendix B.

¹¹⁰³ L1 Jets

¹¹⁰⁴ B.1. Jet matching efficiencies

¹¹⁰⁵ The single jet turn-on curves are derived from events independent of whether the leading
¹¹⁰⁶ jet in an event is matched to a Level 1 jet using ΔR matching detailed in Section (3.4.3)
¹¹⁰⁷ or not. These turn-ons are produced from events which are not triggered on jet quantities
¹¹⁰⁸ and therefore it is not guaranteed that the lead jet of an event will be seeded by a Level
¹¹⁰⁹ 1 jet. Figure B.1 shows the particular matching efficiency of a lead jet to a L1 jet.

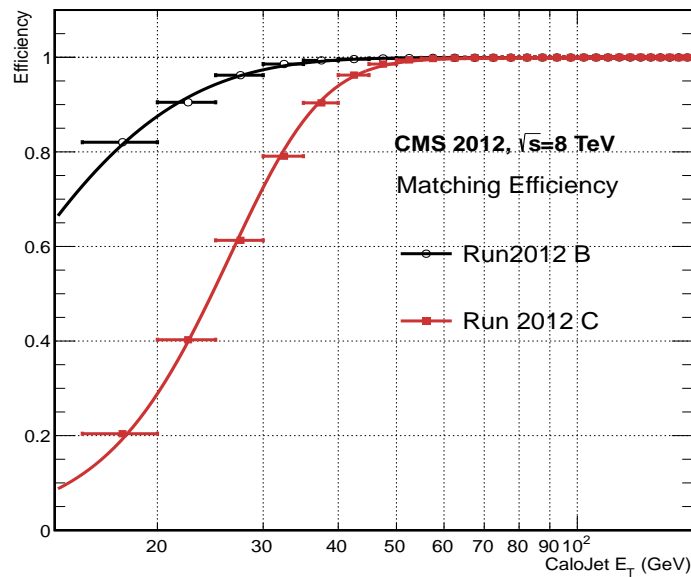


Figure B.1.: Leading jet matching efficiency as a function of the offline CaloJet E_T , measured in an isolated muon triggered dataset in the 2012B and 2012C run periods.

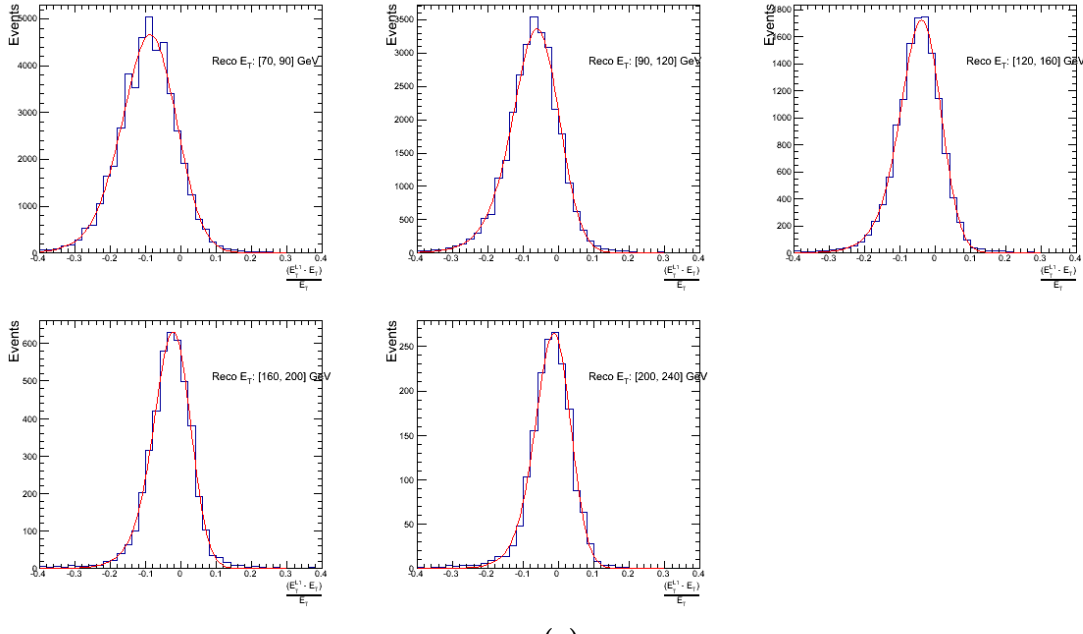
Run Period	μ	σ
2012B	6.62 ± 0.01	0.79 ± 0.03
2012C	19.51 ± 0.03	7.14 ± 0.02

Table B.1.: Results of a cumulative EMG function fit to the turn-on curves for the matching efficiency of the leading jet in an event to a Level-1 jet in run 2012C and 2012B data, measured in an isolated muon triggered sample. The turn-on point, μ , and resolution, σ , are measured with respect to offline Calo Jet E_T .

It can be seen that the turn on is sharper during the 2012B run period. The seed threshold requirement of a 5 GeV jet seed in run 2012C results in more events in which even the lead offline jet does not have an associated L1 jet. For larger jet E_T thresholds, typical of thresholds used in physics analyses, 100% efficiency is observed.

The matching efficiencies have a μ values of 6.62 GeV and 19.51 GeV for Run 2012B and 2012C respectively and is shown in Table B.1.

B.2. Leading Jet Energy Resolution



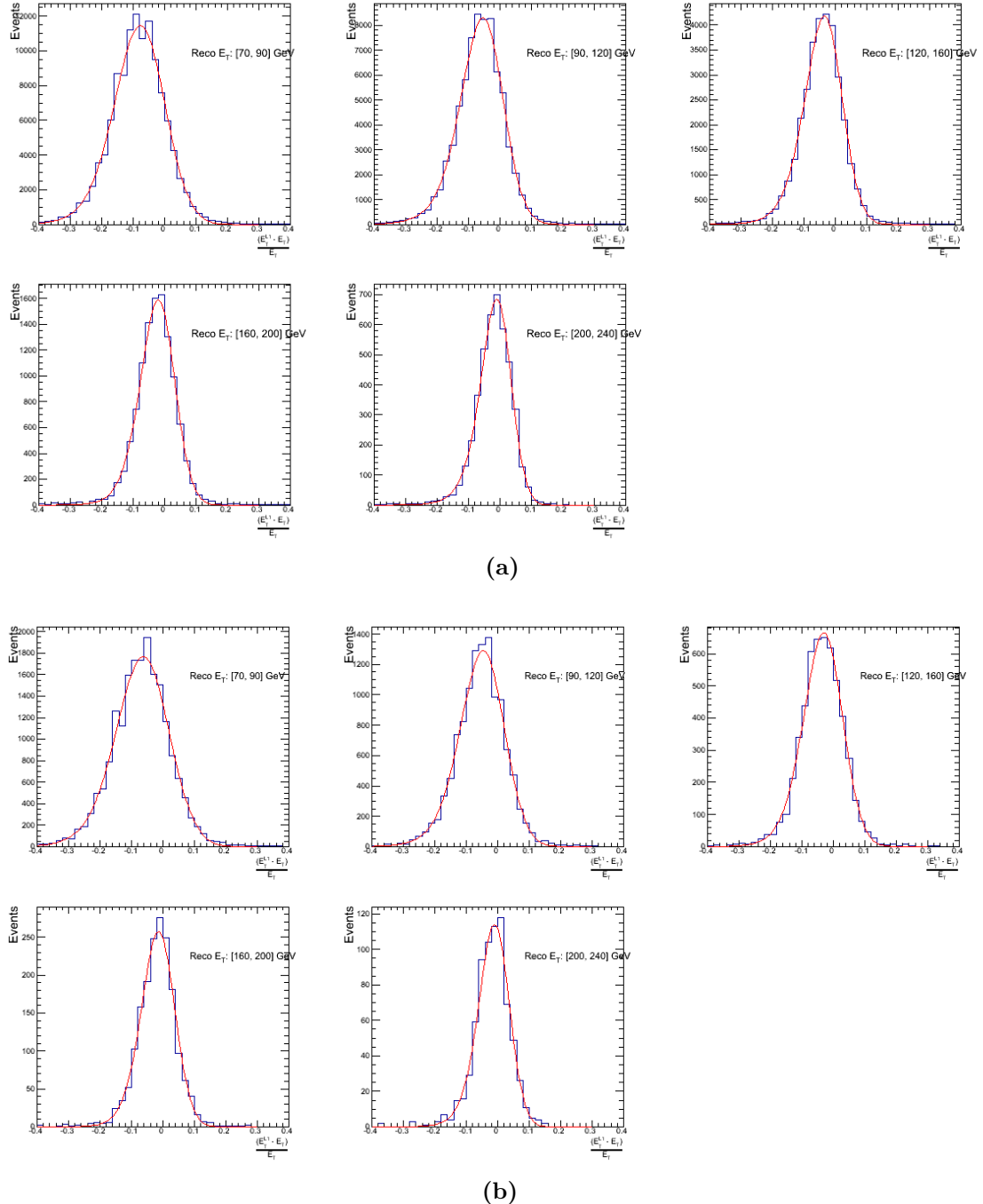
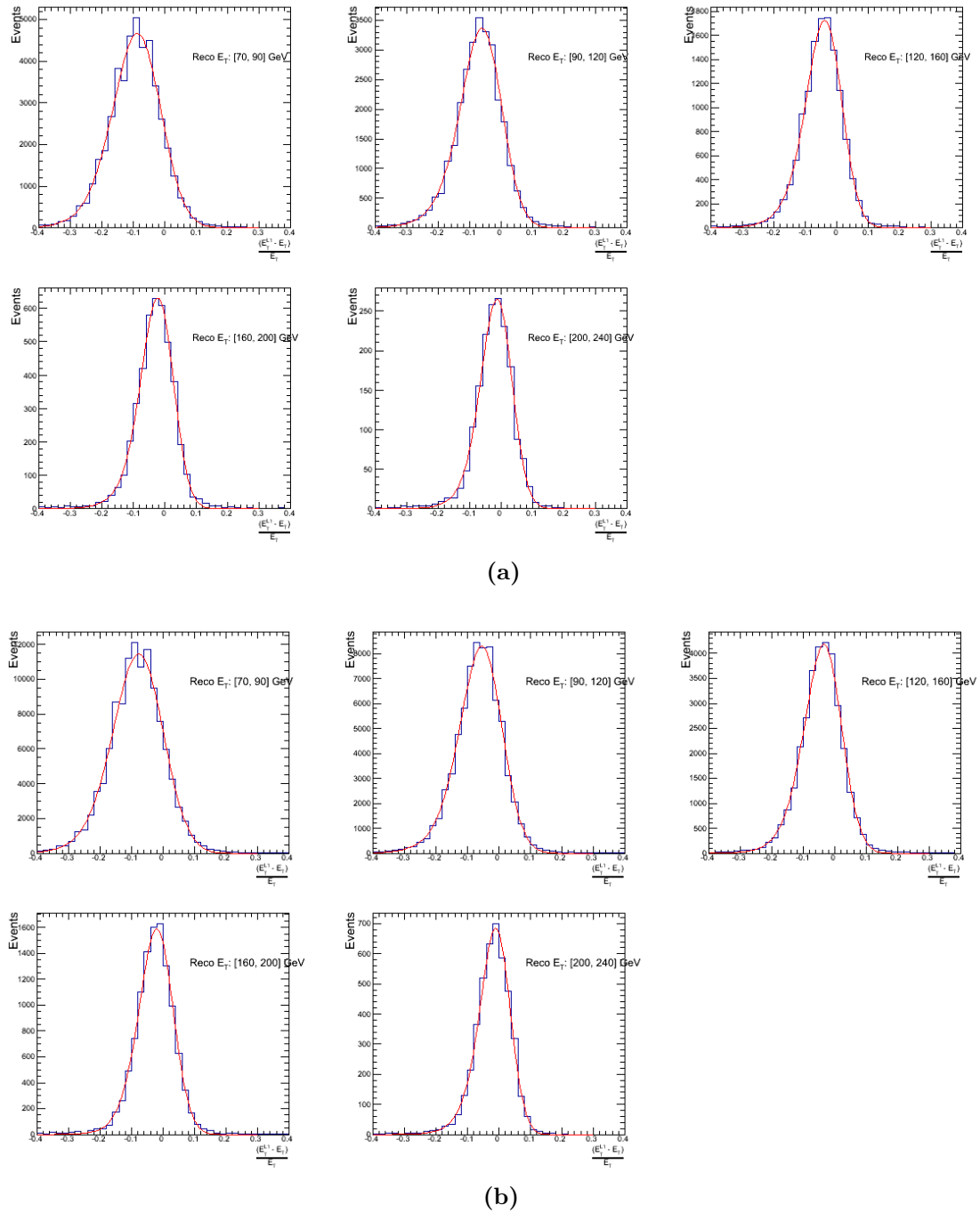
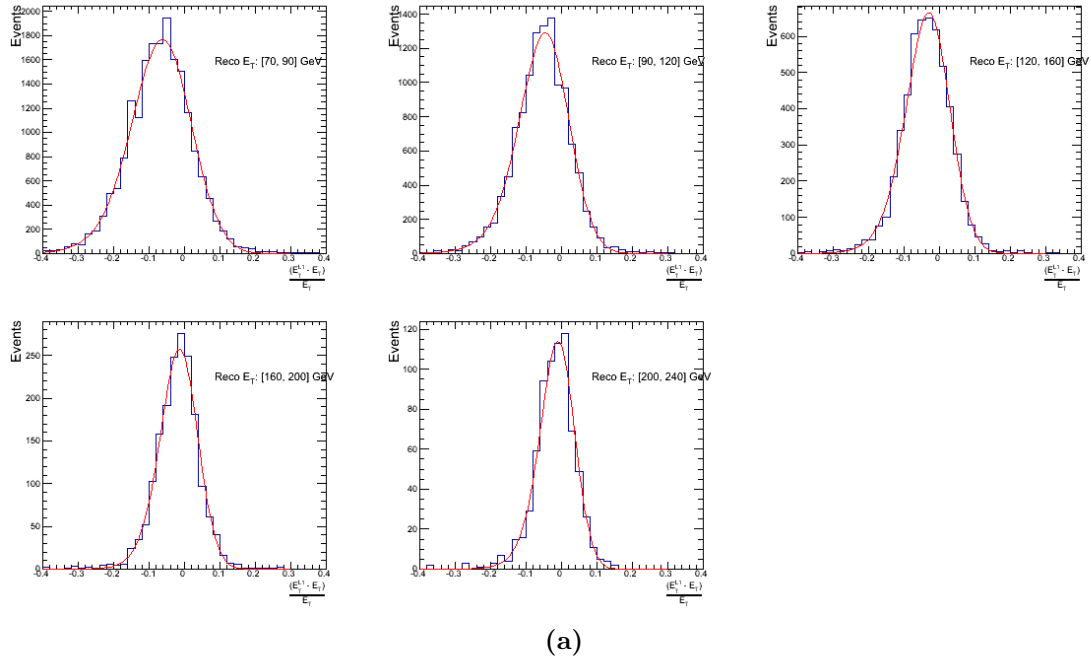


Figure B.2.: Resolution plots of the leading offline jet Calo E_T measured as a function of $\frac{(E_T^{\text{L1}} - E_T^{\text{off}})}{E_T^{\text{off}}}$ for low (a), medium (b) and high (c) pile-up conditions.





(a)

Figure B.3.: Resolution plots of the leading offline jet PF E_T measured as a function of $\frac{(L1 E_T - Offline E_T)}{Offline E_T}$ for low (a), medium (b) and high (c) pile-up conditions.

1117 B.3. Resolution for Energy Sum Quantities

1118 The following plots show the resolution parameters for the four energy sum quantities as
 1119 a function of the quantity (q) itself. In this case, The mean and RMS of the individual
 1120 $\frac{(L1 q - Offline q)}{Offline q}$ distributions, in bins of the quantity q is displayed.

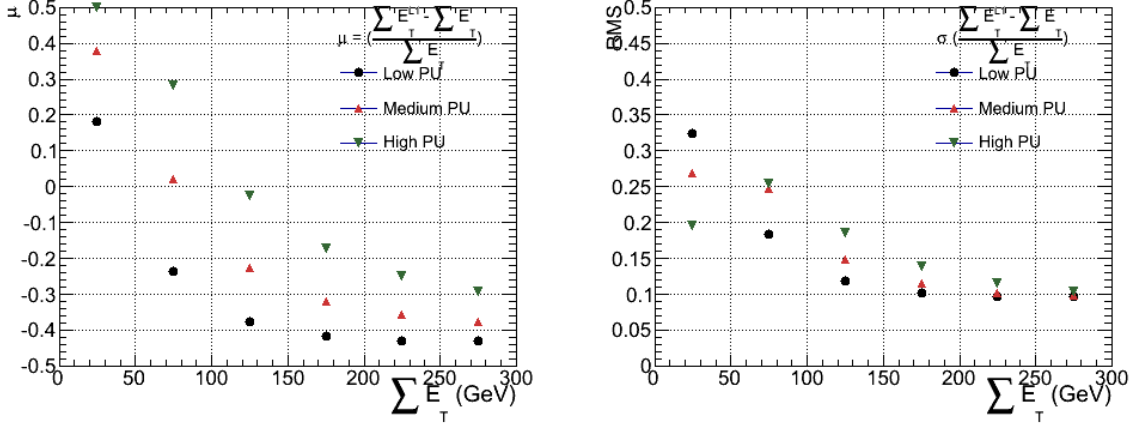


Figure B.4.: $\sum E_T$ resolution parameters in bins of Calo $\sum E_T$ measured for the defined low, medium and high pile up conditions. The plots show the mean μ (left), resolution σ (RMS) of the $\frac{\Delta q}{q}$ distributions.

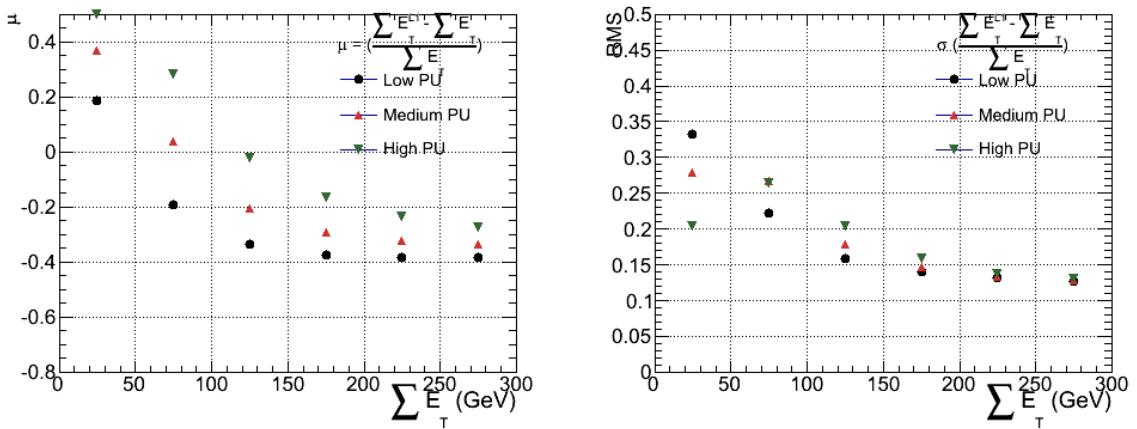


Figure B.5.: $\sum E_T$ resolution parameters in bins of PF $\sum E_T$ measured for the defined low, medium and high pile up conditions. The plots show the mean μ (left), resolution σ (RMS) of the $\frac{\Delta q}{q}$ distributions.

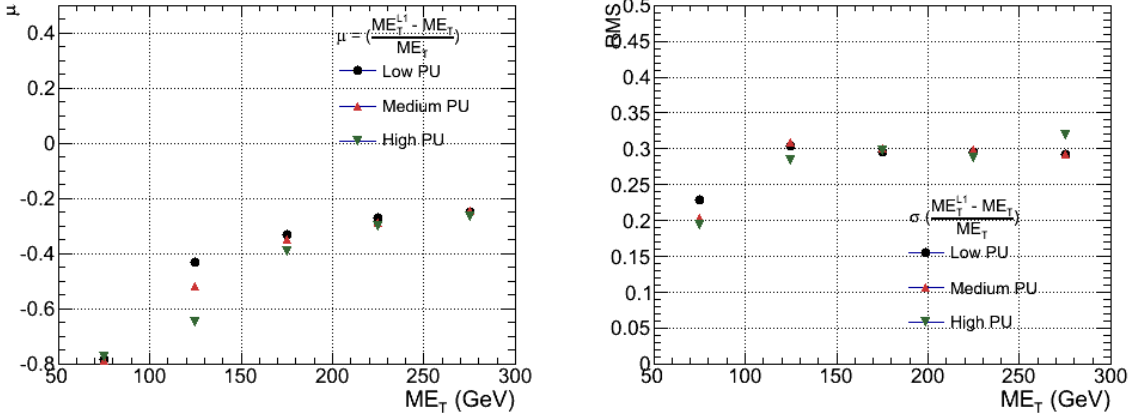


Figure B.6.: \mathcal{E}_T resolution parameters in bins of Calo \mathcal{E}_T measured for the defined low, medium and high pile up conditions. The plots show the mean μ (left), resolution σ (RMS) of the $\frac{\Delta q}{q}$ distributions.

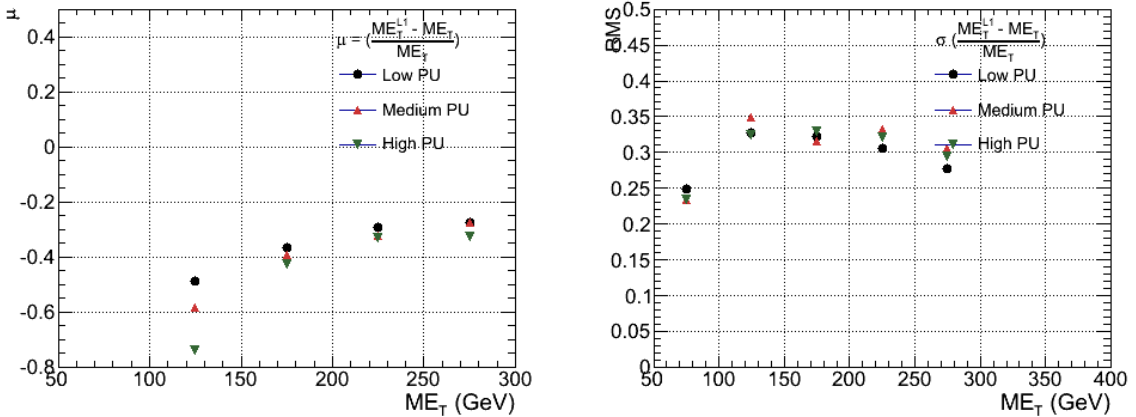


Figure B.7.: \mathcal{E}_T resolution parameters in bins of PF \mathcal{E}_T measured for the defined low, medium and high pile up conditions. The plots show the mean μ (left), resolution σ (RMS) of the $\frac{\Delta q}{q}$ distributions.

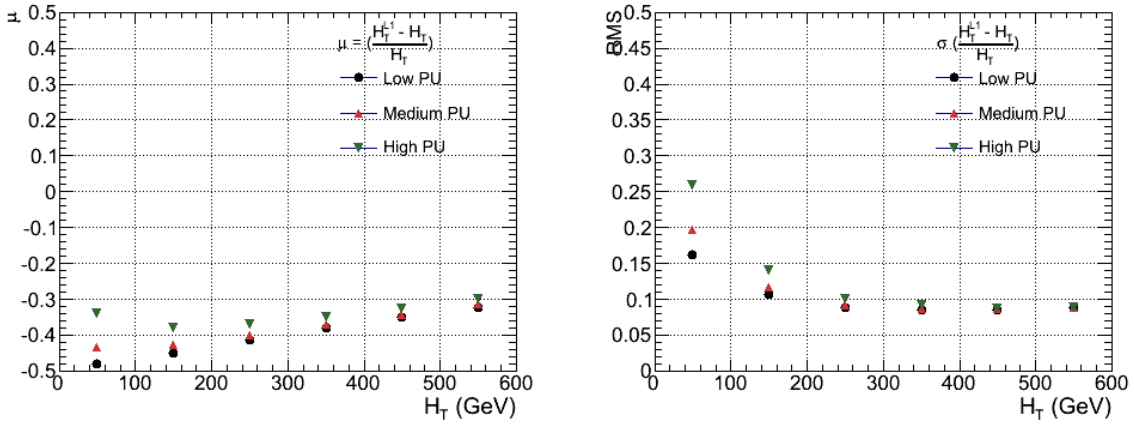


Figure B.8.: H_T resolution parameters in bins of Calo H_T measured for the defined low, medium and high pile up conditions. The plots show the mean μ (left), resolution σ (RMS) of the $\frac{\Delta q}{q}$ distributions.

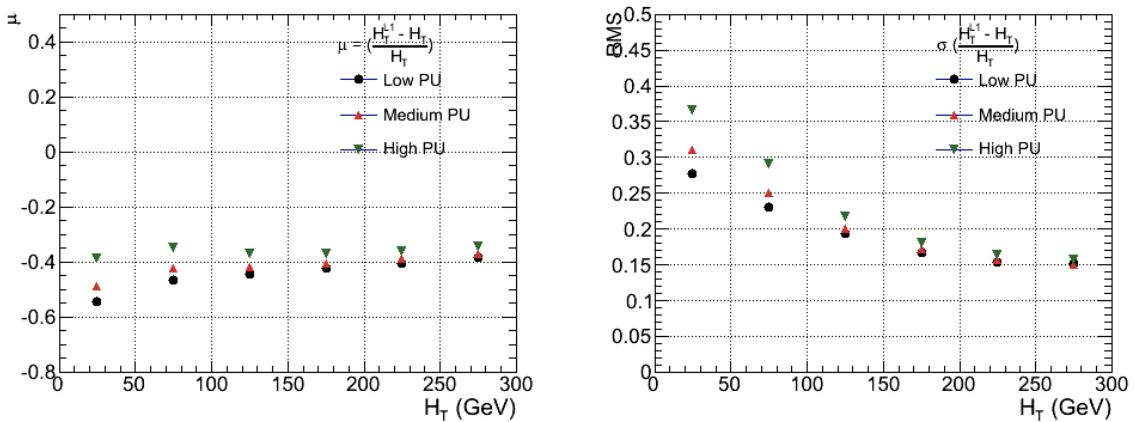


Figure B.9.: H_T resolution parameters in bins of PF H_T measured for the defined low, medium and high pile up conditions. The plots show the mean μ (left), resolution σ (RMS) of the $\frac{\Delta q}{q}$ distributions.

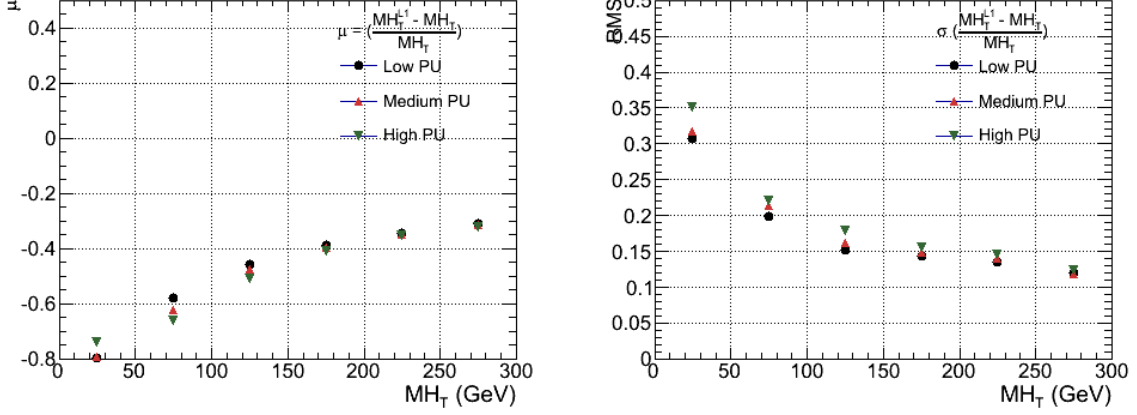


Figure B.10.: H_T resolution parameters in bins of H_T measured for the defined low, medium and high pile up conditions. The plots show the mean μ (left), resolution σ (RMS) of the $\frac{\Delta q}{q}$ distributions.

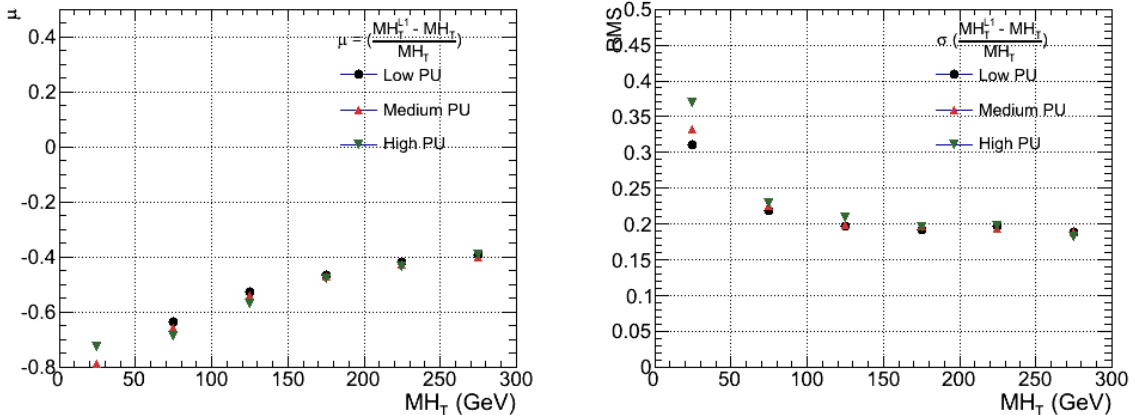


Figure B.11.: H_T resolution parameters in bins of PF H_T measured for the defined low, medium and high pile up conditions. The plots show the mean μ (left), resolution σ (RMS) of the $\frac{\Delta q}{q}$ distributions.

¹¹²² Bibliography

- ¹¹²³ [1] J. Beringer *et al.*, “Review of Particle Physics (RPP),” *Phys.Rev.*, vol. D86, p. 010001, 2012.
- ¹¹²⁴
- ¹¹²⁵ [2] G. H. et al., “Nine-year wilkinson microwave anisotropy probe (wmap) observations: Cosmological parameter results,” *The Astrophysical Journal Supplement Series*, vol. 208, no. 2, p. 19, 2013.
- ¹¹²⁶
- ¹¹²⁷
- ¹¹²⁸ [3] G. Aad *et al.*, “Observation of a new particle in the search for the Standard Model Higgs boson with the ATLAS detector at the LHC,” *Phys.Lett.*, vol. B716, pp. 1–29, 2012.
- ¹¹²⁹
- ¹¹³⁰
- ¹¹³¹ [4] S. Chatrchyan *et al.*, “Observation of a new boson at a mass of 125 GeV with the CMS experiment at the LHC,” *Phys.Lett.*, vol. B716, pp. 30–61, 2012.
- ¹¹³²
- ¹¹³³ [5] S. Chatrchyan *et al.*, “Search for supersymmetry in hadronic final states with missing transverse energy using the variables AlphaT and b-quark multiplicity in pp collisions at 8 TeV,” *Eur.Phys.J.*, vol. C73, p. 2568, 2013.
- ¹¹³⁴
- ¹¹³⁵
- ¹¹³⁶ [6] S. Weinberg, “A model of leptons,” *Phys. Rev. Lett.*, vol. 19, pp. 1264–1266, Nov 1967.
- ¹¹³⁷
- ¹¹³⁸ [7] S. Glashow, “Partial Symmetries of Weak Interactions,” *Nucl.Phys.*, vol. 22, pp. 579–588, 1961.
- ¹¹³⁹
- ¹¹⁴⁰ [8] A. Salam, “Weak and Electromagnetic Interactions,” *Conf.Proc.*, vol. C680519, pp. 367–377, 1968.
- ¹¹⁴¹
- ¹¹⁴² [9] G. Hooft, “Renormalizable lagrangians for massive yang-mills fields,” *Nuclear Physics B*, vol. 35, no. 1, pp. 167 – 188, 1971.
- ¹¹⁴³
- ¹¹⁴⁴ [10] F. Hasert *et al.*, “Observation of Neutrino Like Interactions Without Muon Or Electron in the Gargamelle Neutrino Experiment,” *Phys.Lett.*, vol. B46, pp. 138–140, 1973.
- ¹¹⁴⁵
- ¹¹⁴⁶

- 1147 [11] G. Arnison *et al.*, “Experimental Observation of Lepton Pairs of Invariant Mass
1148 Around 95-GeV/c**2 at the CERN SPS Collider,” *Phys.Lett.*, vol. B126, pp. 398–410,
1149 1983.
- 1150 [12] M. Banner *et al.*, “Observation of Single Isolated Electrons of High Transverse
1151 Momentum in Events with Missing Transverse Energy at the CERN anti-p p
1152 Collider,” *Phys.Lett.*, vol. B122, pp. 476–485, 1983.
- 1153 [13] E. Noether, “Invariante variationsprobleme,” *Nachrichten von der Gesellschaft
1154 der Wissenschaften zu Gttingen, Mathematisch-Physikalische Klasse*, vol. 1918,
1155 pp. 235–257, 1918.
- 1156 [14] F. Halzen and A. D. Martin, “Quarks and leptons.” Wiley, 1985.
- 1157 [15] *Introduction to Elementary Particles*. Wiley-VCH, 2nd ed., Oct. 2008.
- 1158 [16] C. S. Wu, E. Ambler, R. W. Hayward, D. D. Hoppes, and R. P. Hudson, “Ex-
1159 perimental Test of Parity Conservation in Beta Decay,” *Physical Review*, vol. 105,
1160 pp. 1413–1415, Feb. 1957.
- 1161 [17] P. Higgs, “Broken symmetries, massless particles and gauge fields,” *Physics Letters*,
1162 vol. 12, no. 2, pp. 132 – 133, 1964.
- 1163 [18] F. Englert and R. Brout, “Broken symmetry and the mass of gauge vector mesons,”
1164 *Phys. Rev. Lett.*, vol. 13, pp. 321–323, Aug 1964.
- 1165 [19] P. W. Higgs, “Broken symmetries and the masses of gauge bosons,” *Phys. Rev. Lett.*,
1166 vol. 13, pp. 508–509, Oct 1964.
- 1167 [20] G. S. Guralnik, C. R. Hagen, and T. W. B. Kibble, “Global conservation laws and
1168 massless particles,” *Phys. Rev. Lett.*, vol. 13, pp. 585–587, Nov 1964.
- 1169 [21] S. Weinberg, “A model of leptons,” *Phys. Rev. Lett.*, vol. 19, pp. 1264–1266, Nov
1170 1967.
- 1171 [22] H. Yukawa, “On the interaction of elementary particles. i,” *Progress of Theoretical
1172 Physics Supplement*, vol. 1, pp. 1–10, 1955.
- 1173 [23] Y. e. a. Fukuda, “Evidence for oscillation of atmospheric neutrinos,” *Phys. Rev.
1174 Lett.*, vol. 81, pp. 1562–1567, Aug 1998.
- 1175 [24] R. Becker-Szendy, C. Bratton, D. Casper, S. Dye, W. Gajewski, *et al.*, “A Search
1176 for muon-neutrino oscillations with the IMB detector,” *Phys.Rev.Lett.*, vol. 69,

- ₁₁₇₇ pp. 1010–1013, 1992.
- ₁₁₇₈ [25] S. P. Martin, “A Supersymmetry primer,” 1997.
- ₁₁₇₉ [26] H. Nilles, *Supersymmetry, Supergravity and Particle Physics*. Physics reports, North-Holland Physics Publ., 1984.
- ₁₁₈₁ [27] H. E. Haber and G. L. Kane, “The Search for Supersymmetry: Probing Physics Beyond the Standard Model,” *Phys.Rept.*, vol. 117, pp. 75–263, 1985.
- ₁₁₈₃ [28] E. Witten, “Dynamical Breaking of Supersymmetry,” *Nucl.Phys.*, vol. B188, p. 513, 1981.
- ₁₁₈₅ [29] J. Wess and B. Zumino, “Supergauge transformations in four dimensions,” *Nuclear Physics B*, vol. 70, no. 1, pp. 39 – 50, 1974.
- ₁₁₈₇ [30] H. Muller-Kirsten and A. Wiedemann, *Introduction to Supersymmetry*. World Scientific lecture notes in physics, World Scientific, 2010.
- ₁₁₈₉ [31] I. Aitchison, *Supersymmetry in Particle Physics: An Elementary Introduction*. Cambridge University Press, 2007.
- ₁₁₉₁ [32] K. A. Intriligator and N. Seiberg, “Lectures on Supersymmetry Breaking,” *Class.Quant.Grav.*, vol. 24, pp. S741–S772, 2007.
- ₁₁₉₃ [33] Y. Shadmi, “Supersymmetry breaking,” pp. 147–180, 2006.
- ₁₁₉₄ [34] C. Burgess, P. G. Camara, S. de Alwis, S. Giddings, A. Maharana, *et al.*, “Warped Supersymmetry Breaking,” *JHEP*, vol. 0804, p. 053, 2008.
- ₁₁₉₆ [35] H. Murayama, “Supersymmetry breaking made easy, viable, and generic,” 2007.
- ₁₁₉₇ [36] H. Baer and X. Tata, *Weak Scale Supersymmetry: From Superfields to Scattering Events*. Cambridge University Press, 2006.
- ₁₁₉₉ [37] S. P. Martin, “Implications of supersymmetric models with natural r-parity conservation,” 1996.
- ₁₂₀₁ [38] G. L. Kane, C. F. Kolda, L. Roszkowski, and J. D. Wells, “Study of constrained minimal supersymmetry,” *Phys.Rev.*, vol. D49, pp. 6173–6210, 1994.
- ₁₂₀₃ [39] C. Stlege, G. Bertone, D. Cerdeno, M. Fornasa, R. Ruiz de Austri, *et al.*, “Updated global fits of the cmSSM including the latest LHC SUSY and Higgs searches and XENON100 data,” *JCAP*, vol. 1203, p. 030, 2012.

- 1206 [40] M. Citron, J. Ellis, F. Luo, J. Marrouche, K. Olive, *et al.*, “The End of the CMSSM
1207 Coannihilation Strip is Nigh,” *Phys.Rev.*, vol. D87, p. 036012, 2013.
- 1208 [41] D. Ghosh, M. Guchait, S. Raychaudhuri, and D. Sengupta, “How Constrained is
1209 the cMSSM?,” *Phys.Rev.*, vol. D86, p. 055007, 2012.
- 1210 [42] D. Alves *et al.*, “Simplified Models for LHC New Physics Searches,” *J.Phys.*, vol. G39,
1211 p. 105005, 2012.
- 1212 [43] J. Alwall, P. Schuster, and N. Toro, “Simplified Models for a First Characterization
1213 of New Physics at the LHC,” *Phys.Rev.*, vol. D79, p. 075020, 2009.
- 1214 [44] S. Chatrchyan *et al.*, “Interpretation of Searches for Supersymmetry with simplified
1215 Models,” *Phys.Rev.*, vol. D88, p. 052017, 2013.
- 1216 [45] J. Hisano, K. Kurosawa, and Y. Nomura, “Natural effective supersymmetry,”
1217 *Nucl.Phys.*, vol. B584, pp. 3–45, 2000.
- 1218 [46] M. Papucci, J. T. Ruderman, and A. Weiler, “Natural SUSY Endures,” *JHEP*,
1219 vol. 1209, p. 035, 2012.
- 1220 [47] B. Allanach and B. Gripaios, “Hide and Seek With Natural Supersymmetry at the
1221 LHC,” *JHEP*, vol. 1205, p. 062, 2012.
- 1222 [48] K. Aamodt *et al.*, “The ALICE experiment at the CERN LHC,” *JINST*, vol. 3,
1223 p. S08002, 2008.
- 1224 [49] G. Aad *et al.*, “The ATLAS Experiment at the CERN Large Hadron Collider,”
1225 *JINST*, vol. 3, 2008.
- 1226 [50] R. Adolphi *et al.*, “The cms experiment at the cern lhc,” *JINST*, vol. 0803, p. S08004,
1227 2008.
- 1228 [51] A. A. Alves *et al.*, “The LHCb Detector at the LHC,” *JINST*, vol. 3, p. S08005,
1229 2008.
- 1230 [52] J.-L. Caron, “Lhc layout.. schema general du lhc..” Sep 1997.
- 1231 [53] C. Collaboration, “Cms luminosity - public results.”
1232 twiki.cern.ch/twiki/bin/view/CMSPublic/LumiPublicResults., 2011.
- 1233 [54] CERN, “Cms compact muon solenoid..” <http://public.web.cern.ch/public/Objects/LHC/CMSnc.jpg>
1234 Feb 2010.

- 1235 [55] *The CMS electromagnetic calorimeter project: Technical Design Report*. Technical
1236 Design Report CMS, Geneva: CERN, 1997.
- 1237 [56] *The CMS muon project: Technical Design Report*. Technical Design Report CMS,
1238 Geneva: CERN, 1997.
- 1239 [57] CMS Collaboration, “The cms physics technical design report, volume 1,”
1240 *CERN/LHCC*, vol. 2006-001, 2006.
- 1241 [58] M. Cacciari, G. P. Salam, and G. Soyez, “The anti- k_t jet clustering algorithm,”
1242 *Journal of High Energy Physics*, vol. 2008, no. 04, p. 063, 2008.
- 1243 [59] “Jet performance in pp collisions at 7 tev,” Tech. Rep. CMS-PAS-JME-10-003,
1244 CERN, Geneva, 2010.
- 1245 [60] X. Janssen, “Underlying event and jet reconstruction in cms,” Tech. Rep. CMS-CR-
1246 2011-012, CERN, Geneva, Jan 2011.
- 1247 [61] T. C. collaboration, “Determination of jet energy calibration and transverse mo-
1248 mentum resolution in cms,” *Journal of Instrumentation*, vol. 6, no. 11, p. P11002,
1249 2011.
- 1250 [62] R. Eusebi and on behalf of the CMS collaboration), “Jet energy corrections and
1251 uncertainties in cms: reducing their impact on physics measurements,” *Journal of
1252 Physics: Conference Series*, vol. 404, no. 1, p. 012014, 2012.
- 1253 [63] “Performance of b tagging at $\sqrt{s}=8$ tev in multijet, ttbar and boosted topology
1254 events,” no. CMS-PAS-BTV-13-001, 2013.
- 1255 [64] T. C. collaboration, “Identification of b-quark jets with the cms experiment,” *Journal
1256 of Instrumentation*, vol. 8, no. 04, p. P04013, 2013.
- 1257 [65] S. Dasu *et al.*, “CMS. The TriDAS project. Technical design report, vol. 1: The
1258 trigger systems,” 2000.
- 1259 [66] P. Sphicas, “CMS: The TriDAS project. Technical design report, Vol. 2: Data
1260 acquisition and high-level trigger,” 2002.
- 1261 [67] J. B. et al., “Calibration and Performance of the Jets and Energy Sums in the
1262 Level-1 Trigger ,” no. CMS IN 2013/006 (2013), 2013.
- 1263 [68] B. et al., “Study of Level-1 Trigger Jet Performance in High Pile-up Running
1264 Conditions,” no. CMS IN 2013/007 (2013), 2013.

- ₁₂₆₅ [69] J. J. Brooke, “Performance of the cms level-1 trigger,” Tech. Rep. CMS-CR-2012-322.
₁₂₆₆ CERN-CMS-CR-2012-322, CERN, Geneva, Nov 2012.
- ₁₂₆₇ [70] L. Randall and D. Tucker-Smith, “Dijet searches for supersymmetry at the large
₁₂₆₈ hadron collider,” *Phys. Rev. Lett.*, vol. 101, p. 221803, Nov 2008.
- ₁₂₆₉ [71] “SUSY searches with dijet events,” 2008.
- ₁₂₇₀ [72] “Search strategy for exclusive multi-jet events from supersymmetry at CMS,” Tech.
₁₂₇₁ Rep. CMS-PAS-SUS-09-001, CERN, 2009. Geneva, Jul 2009.

1272 Acronyms

- 1273 ALICE** A Large Ion Collider Experiment
- 1274 ATLAS** A Toroidal LHC ApparatuS
- 1275 APD** Avalanche Photo-Diodes
- 1276 BSM** Beyond Standard Model
- 1277 CERN** European Organization for Nuclear Research
- 1278 CMS** Compact Muon Solenoid
- 1279 CMSSM** Compressed Minimal SuperSymmetric Model
- 1280 CSC** Cathode Stripe Chamber
- 1281 CSV** Combined Secondary Vertex
- 1282 CSVM** Combined Secondary Vertex Medium Working Point
- 1283 DT** Drift Tube
- 1284 ECAL** Electromagnetic CALorimeter
- 1285 EB** Electromagnetic CALorimeter Barrel
- 1286 EE** Electromagnetic CALorimeter Endcap
- 1287 ES** Electromagnetic CALorimeter pre-Shower
- 1288 EMG** Exponentially Modified Gaussian
- 1289 EPJC** European Physical Journal C
- 1290 EWK** Electroweak Sector
- 1291 GCT** Global Calorimeter Trigger
- 1292 GMT** Global MuonTrigger
- 1293 GT** Global Trigger
- 1294 HB** Hadron Barrel
- 1295 HE** Hadron Endcaps

1296	HF	Hadron Forward
1297	HO	Hadron Outer
1298	HCAL	Hadronic CALorimeter
1299	HLT	Higher Level Trigger
1300	LUT	Look Up Table
1301	L1	Level 1 Trigger
1302	LHC	Large Hadron Collider
1303	LHCb	Large Hadron Collider Beauty
1304	LSP	Lightest Supersymmetric Partner
1305	PS	Proton Synchrotron
1306	QED	Quantum Electro-Dynamics
1307	QCD	Quantum Chromo-Dynamics
1308	QFT	Quantum Field Theory
1309	RPC	Resistive Plate Chamber
1310	RCT	Regional Calorimeter Trigger
1311	RMT	Regional Muon Trigger
1312	SUSY	SUperSYmmetry
1313	SM	Standard Model
1314	SMS	Simplified Model Spectra
1315	SPS	Super Proton Synchrotron
1316	VEV	Vacuum Expectation Value
1317	VPT	Vacuum Photo-Triodes
1318	WIMP	Weakly Interacting Massive Particle